



PAUL SCHERRER INSTITUT



PSI Bericht Nr. 97-06

Juni 1997

ISSN 1019-0643

Labor für Radio- und Umweltchemie

**Cosmogenic Radionuclides in the Environment:
³²Si in Precipitation Samples from the Jungfraujoch,
Production Cross Sections of ³⁶Cl in Argon and
Modeling of the Atmospheric ³⁶Cl Production**

Yves Parrat

**Cosmogenic Radionuclides in the Environment:
³²Si in Precipitation Samples from the Jungfraujoch,
Production Cross Sections of ³⁶Cl in Argon and
Modeling of the Atmospheric ³⁶Cl Production**

Yves Parrat

June 1997

Ph. D. Thesis, University of Berne

To René Cattin, my grandfather

Contents

Summary	5
1. Introduction	6
1.1 Production of cosmogenic isotopes in the earth atmosphere	6
1.2 Spatial variations of the cosmic ray flux	7
1.3 Temporal variations of the cosmic ray flux	8
1.4 Archives of cosmogenic isotopes	9
1.5 Other sources of production	10
1.6 Application of cosmogenic nuclides as tracers	10
1.7 Accelerator Mass Spectrometry	11
1.8 Outline of this work	12
2. ^{32}Si in fresh snow samples from the Jungfraujoch	13
2.1 The half-life of ^{32}Si	14
2.2 Experimental	15
2.3 Results and discussion	16
2.4 Conclusion	19
3. Measurements of proton induced cross sections in gas targets	21
3.1 The irradiation facilities	22
3.2 The gas target	23
3.3 The proton dose measurements	24
3.3.1 Monitoring using a Monte-Carlo simulation	25
3.3.2 Monitoring with Faraday-cup - ionization chamber calibration curve	27
3.3.3 Monitoring with the reaction $^{27}\text{Al}(p,3p3n)^{22}\text{Na}$	29
3.3.4 Comparison of the results	32
3.4 Treatment of the target after irradiation	33
3.5 Results and discussion	37
3.5.1 Proton induced cross sections on nickel targets	37
3.5.2 Proton induced cross sections in gas targets	42
3.6 Conclusions	46

4.	Atmospheric production rate of ^{36}Cl	47
4.1	Calculation of the atmospheric production rate of ^{36}Cl	47
4.2	Deposition rates of ^{36}Cl	56
4.3	Conclusions	57
	References	58
	Acknowledgements	65
	Curriculum vitae	66

Summary

The concentrations of the cosmogenic radionuclide ^{32}Si were measured in four fresh snow samples from the Jungfrauoch in the Swiss Alps (3450 m. asl.) to study the feasibility of measuring this potential dating nuclide with Accelerator Mass Spectrometry. This technique could reduce drastically the amount of material needed for measurements of ^{32}Si concentrations in environmental samples in contrast to conventional radiometric detection. The measured ^{32}Si concentrations in the snow samples were between 1.84 and 6.28 $\mu\text{Bq l}^{-1}$. These values agree with other measurements of precipitation samples. The measured $^{32}\text{Si}/\text{Si}_{\text{tot}}$ ratios ranged from $2.5 \cdot 10^{-17}$ to $2.3 \cdot 10^{-15}$ and were thus below the present AMS detection limit of about 10^{-14} , showing that at present it is not possible to carry out AMS measurements of ^{32}Si in precipitation samples.

For the first time, experimental cross sections of the reaction $^{40}\text{Ar}(p,X)^{36}\text{Cl}$ have been determined for the proton energy range 16-590 MeV. These cross sections were measured using a gas target, a novel method which was tested successfully by irradiating nitrogen targets to confirm literature values of the $\text{N}(p,X)^7\text{Be}$ and $\text{N}(p,X)^{10}\text{Be}$ cross sections. In fact, good agreement was found between the obtained cross sections with those using solid targets. Production of several radionuclides in the reaction of proton with nickel were also measured. Comparison of these cross sections with literature data proved that the proton flux measurements carried out with ionization chambers were very accurate. The excitation function of the reaction $^{40}\text{Ar}(p,X)^{36}\text{Cl}$ exhibits two maxima, at proton energies of 20 MeV for the $(p,\alpha n)$ reaction and 95 MeV for the $(p,2p3n)$ reaction, with maximum cross sections of 105 mb and 53 mb, respectively.

A new calculation of the ^{36}Cl production rate was performed based on the measured $^{40}\text{Ar}(p,X)^{36}\text{Cl}$ cross sections. Using a Monte-Carlo simulation of the proton and neutron intensities in the atmosphere (Flückiger, 1976), an average production rate of 20 ^{36}Cl atoms/ m^2s was found. This value agrees with an earlier estimate by Oeschger et al. (1969) and with a recent value obtained by Huggle et al. (1996), but is two times higher than the mostly used value of Lal and Peters (1967). The deduced production rate was used to predict the ^{36}Cl deposition rate as a function of the latitude. The resulting prediction is however not in satisfactory agreement with measured deposition rates (Synal et al., 1994; Synal, 1997).

1. Introduction

1.1 Production of cosmogenic isotopes in the earth atmosphere

The earth atmosphere is exposed to cosmic radiation, which can be divided into two main components: the galactic cosmic rays (GCR) and the solar cosmic rays (SCR). GCR are produced during supernovae explosions, whereas SCR originate from solar flares. The two types of cosmic rays consist mainly of protons (about 90%), α -particles (about 10%) and about 1% heavier nuclei. The energy distributions and intensities of these two components differ considerably. Typically, the energy range of the GCR lies between 100 MeV and 10 GeV, with a mean particle flux of about 3 particles/cm²s, whereas the SCR have characteristic energies of 5 to 100 MeV with a flux of about 100 particles/cm²s (Reedy et al., 1983).

After entering the atmosphere, the cosmic rays lose energy through nuclear interactions and ionization processes. These reactions lead to a production of secondary particles (neutrons, electrons, muons, pions, etc.), which may react again so that a cascade of particles is produced. The interaction mean free path λ in the atmosphere of a high energetic primary proton is about 75 g/cm², which corresponds to an average of 12 reactions along a vertical trajectory through the atmosphere (Allkofer and Grieder, 1984). Due to their lower energies, the SCR protons have shorter interaction mean free paths, so that they only react in the upper part of the atmosphere.

Cosmogenic nuclides are produced in the atmosphere through spallation and low energy reactions. Spallation is a nucleon-nucleon interaction, which occurs at incident particle energies above 50 MeV. Due to the high momentum of the incident particle, several particles are directly emitted from the target nucleus. The residual excited nucleus then decays through fragmentation or particle emission. Low energy reactions can be described as reactions, where the incident particle is "absorbed" by the nucleus and its energy distributed among all nucleons, resulting in an excited compound nucleus. The particles, which lead to production of isotopes in the atmosphere are essentially neutrons and, to a lower degree, protons. Muons are mainly responsible for the isotope production in the earth crust, since their mean free path is much higher than that for neutrons and protons. In nuclear reactions, stable isotopes as well as radioisotopes can be produced. The half-lives of the radioisotopes produced in the atmosphere lie between seconds and millions of years. Table 1 gives a summary of the most important radionuclides produced in the atmosphere.

Table 1.1: *Cosmogenic isotopes with half-lives longer than 50 days.*

Isotope	Half-life	Main targets
³ He	stable	N, O
¹⁰ Be	1.6·10 ⁶ y	N, O
²⁶ Al	7.2·10 ⁵ y	Ar
³⁶ Cl	3.0·10 ⁵ y	Ar
¹⁴ C	5730 y	N, O
³⁹ Ar	269 y	Ar
³² Si	135 y ¹	Ar
³ H	12.3 y	N, O
²² Na	2.6 y	Ar
³⁵ S	87.5 d	Ar
⁷ Be	53.3 d	N, O

¹ See chapter 2.1 for detailed information on the half-life of ³²Si

Many factors control the production rate of cosmogenic isotopes. The cosmic ray intensity varies in energy, time and space. The production rate also depends on the reaction cross sections, which are energy dependent, and different for each reaction.

1.2 Spatial variations of the cosmic ray flux

The flux of particles produced by the primary cosmic rays in the atmosphere increases with depth in the first 100 g/cm². After reaching an intensity maximum, it decreases again through absorption and decay processes at a height of about 20 km (Pfozter maximum).

The magnetic field of the earth strongly influences the spatial distribution of cosmic rays. It deflects charged particles as a function of their momentum. The field can be approximated by a dipole, the axis of which today differs by an angle of 11.5° from the axis of the earth rotation (the orientation of the dipole moves with time). The charged particles are more deflected at the geomagnetic equator than at the poles, leading to a decrease of isotope production rate as a function of decreasing latitude. The cut-off rigidity (R_c , in units of GV) expresses the momentum that a charged particle needs to enter the atmosphere at a latitude φ :

$$R_c = \frac{p \cdot c}{e} \quad (1.1)$$

Where: p : momentum of the incident particle [kg·m·s⁻¹]
 c : velocity of the light in vacuum [m·s⁻¹]
 e : charge of the incident particle [C]

For particles entering the atmosphere vertically, the cut-off rigidity varies with $\cos^4\phi$:

$$R_{cv} = \frac{M}{4R^2} \cdot \cos^4 \phi = 14.9 \cdot \cos^4 \phi \quad (1.2)$$

Where: M: Earth's dipole moment [$\text{GV}\cdot\text{m}^2$]
R: Radius of the Earth [m]

For example, a vertical proton should have an energy > 14.0 GeV to enter the atmosphere where the cut-off rigidity is 14.9 GV (geomagnetic equator). This shows that such energies are typical for SCR, e.g. a proton with an energy of 100 MeV can enter the atmosphere only at a latitude $\phi > 65^\circ$.

1.3 Temporal variations of the cosmic ray flux

The strength and orientation of the earth magnetic field varies with time. This induces changes in the intensity and spatial distribution of cosmic rays in the atmosphere.

The magnetic activity of the sun also influences the intensity of the cosmic rays. The sun emits plasma clouds, which expand into the interplanetary space and which induce magnetic fields. This phenomenon is called solar wind. The intensity of the solar wind varies with time and is correlated with the number of sunspots, which varies with an 11 years' cycle (Schwabe cycle). During high sun activity periods, i.e. when the sunspot number is high and consequently the solar wind very intense, the low energy particles of the GCR are deflected in the magnetic field carried by the plasma clouds. As a consequence, the intensity of GCR in the atmosphere is reduced. On the contrary, during periods of low solar activity, the cosmic rays will reach the earth without significant deflection. Periods with very low sunspot activity were observed which led to a high flux of cosmic rays. A well-known period of this type is the Maunder minimum (1645-1715).

The solar flares, which are the main source of SCR, are sporadic events. They are more frequent and intense during periods of high sun activity and typically last some days. Their average value over a solar cycle is about ten events per year. During these short periods, the intensity and energy spectrum of cosmic rays in the atmosphere are highly variable.

1.4 Archives of cosmogenic isotopes

The production of cosmogenic isotopes takes place essentially in the stratosphere - about 2/3 of total production (Lal and Peters, 1967)- and in the upper troposphere. The main part of these nuclides attach to aerosol particles, whereas some of them form gaseous species (for example $^{14}\text{CO}_2$, H^{36}Cl ,...). The residence time of aerosol particles in the stratosphere is about 1 year (Gavini et al., 1974), that of the volatile species being much longer. Short-lived isotopes produced in the stratosphere consequently do not reach the earth surface, the tropospherically produced ones being the only ones reaching the earth. In the troposphere, the cosmogenic nuclides are essentially removed by wet deposition within about two weeks to one month.

The dependence of deposition rates on latitude is different from the one of production rates. The deposition rates of bomb produced ^{90}Sr was practically independent of the latitude even though the activity was introduced into the stratosphere at a well defined place (Machta and List, 1959). The deposition rate is essentially controlled by the discontinuity of the tropopause at mid latitudes, where stratospheric - tropospheric air exchange processes takes place essentially. The deposition rates are also affected by seasonal effects because stratospheric intrusions occur mainly in spring, leading to a higher transfer of cosmogenic nuclides into the troposphere. Figure 1.1 summarizes the processes and controlling factors leading to the deposition of cosmogenic nuclides on any earth archive.

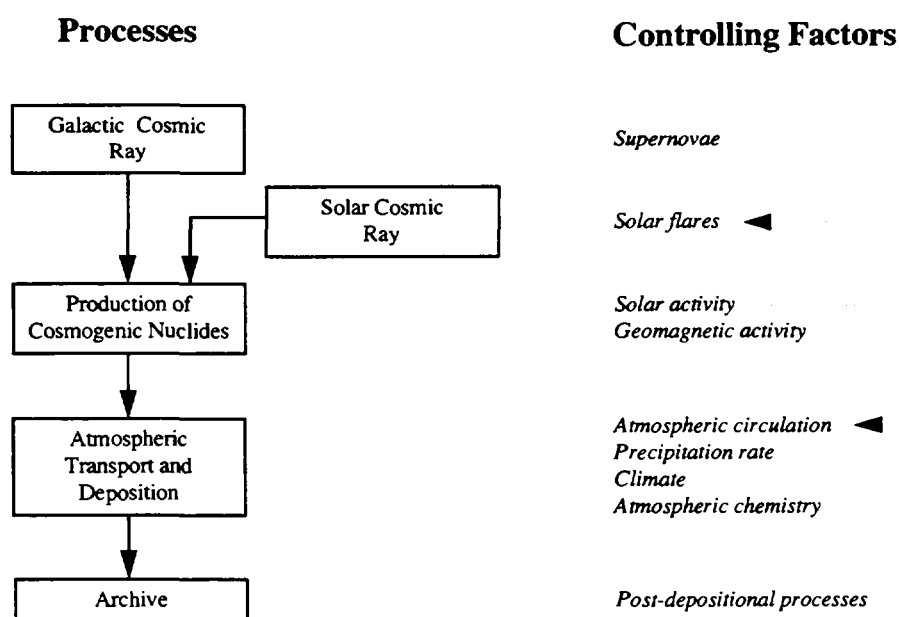


Figure 1.1: Processes controlling the terrestrial distribution of cosmogenic isotopes (from Finkel and Suter, 1993).

1.5 Other sources of production

Some of the isotopes listed in Table 1.1 were also produced during the atmospheric nuclear weapons tests at the end of the 1950's and beginning of the 1960's by interactions of neutrons with bomb material, the atmosphere and, in some cases, seaspray and soil. Small explosions produced fireballs in the troposphere, initiating convective forces which sucked soil particles upward. These particles could then react with neutrons to produce radionuclides.

It is well known that ^3H was produced during these tests, giving new possibilities in using this for dating purposes. The tropospheric content of ^{14}C increased by about 60% above natural levels at the end of the 1960's (Nydal, 1968). Evidence for production of ^{36}Cl is given by Synal et al. (1990): in a Greenland ice core, a peak concentration higher by three orders of magnitude compared to the pre-bomb value was found at the end of the 1950's, caused by the atoll weapons tests. ^{36}Cl is produced through neutron absorption of seasalt chlorine. ^{32}Si was probably also produced by the nuclear weapons tests at the beginning of the 1960's, with a maximum in 1963 (Dansgaard et al., 1966). Lal et al. (1979) gave also evidence of ^{32}Si production, as well as ^{22}Na and ^{35}S , probably through reaction with soil particles.

1.6 Application of cosmogenic nuclides as tracers

Cosmogenic nuclides were used in different tracer applications, depending on their half-life and their occurrence in the studied system. For example, the concentration variations of ^{10}Be and ^{36}Cl in Greenland ice cores as a function of the core depth allowed to reconstruct the history of the sun activity over a very large time scale (Beer et al., 1990). ^7Be , which has a short half-life, was mainly used to study atmospheric transport processes, or more precisely, transport of air masses through the tropopause (Reiter et al., 1983).

The use of cosmogenic nuclides for dating purposes is very difficult because of the spatial and temporal variations of the production rates. Moreover, the different atmospheric chemistry of these nuclides leads to a different dependence of the deposition rate as a function of the latitude. Up to now, only ^{14}C was successfully used in dating applications since it was possible to create calibration curves by measuring the ^{14}C concentration in tree rings dated with dendrochronology. However, the time scale covered by ^{14}C is limited. In addition, since $^{14}\text{CO}_2$ is not deposited by precipitation, the concentration of radiocarbon in some systems such as ice cores or groundwater is very low.

For many applications of cosmogenic nuclides, an accurate modeling of the production rates and deposition rates as a function of latitude and time would be needed. Some production rate

calculations have already been carried out (Lal and Peters, 1967; Oeschger et al., 1969; O'Brien, 1979). However, in many cases, these calculations do not agree with experimental data. At present, only the temporal variability of the production rate is known with high enough accuracy. Efforts are still needed to enhance the knowledge of the reaction cross sections leading to atmospheric production of cosmogenic nuclides. So far, the calculations were carried out with semi-empirical models. Also the knowledge of the atmospheric behavior of cosmogenic nuclides should be improved in order to better predict their deposition rates.

1.7 Accelerator mass spectrometry

Conventional radiometric measurements of some cosmogenic nuclides such as ^{14}C , ^{36}Cl , ^{10}Be or ^{26}Al are difficult due to their long half-lives and the corresponding low decay rates. The introduction of accelerator mass spectrometry (AMS) in 1977 has enlarged considerably the applications of such isotopes in environmental sciences by drastically reducing the amount of material and measuring time needed for a determination. In contrast to conventional methods, which count the number of decaying atoms, AMS measures the ratio of the number concentration of isotopes of an element, e.g. ^{12}C : ^{13}C : ^{14}C in a given sample. This method allows to separate the cosmogenic isotope of an element from their stable isotopes down to a ratio of about 10^{-14} . With AMS, it is possible to measure about 10^6 atoms per sample. Figure 1.2 shows a schematic layout of an AMS facility.

The sample is bombarded with Cs^+ ions to produce a negative ion beam. A first magnetic analyzer allows to select the masses of interest. The negative ions are then accelerated in the first half of a van de Graaf accelerator. The negative ions are then stripped in a gas, loose electrons and become positively charged. The positive ions are further accelerated in the second half of the accelerator. Behind the accelerator, the beam consists of ions of different charges and thus, different energies. An electrostatic deflector allows to select ions with the same energy to charge ratio, and a second magnetic analyzer separates the masses. The ions from the stable isotopes are measured by Faraday cups, whereas the ions of the radioactive isotopes are counted and identified with nuclear counter techniques.

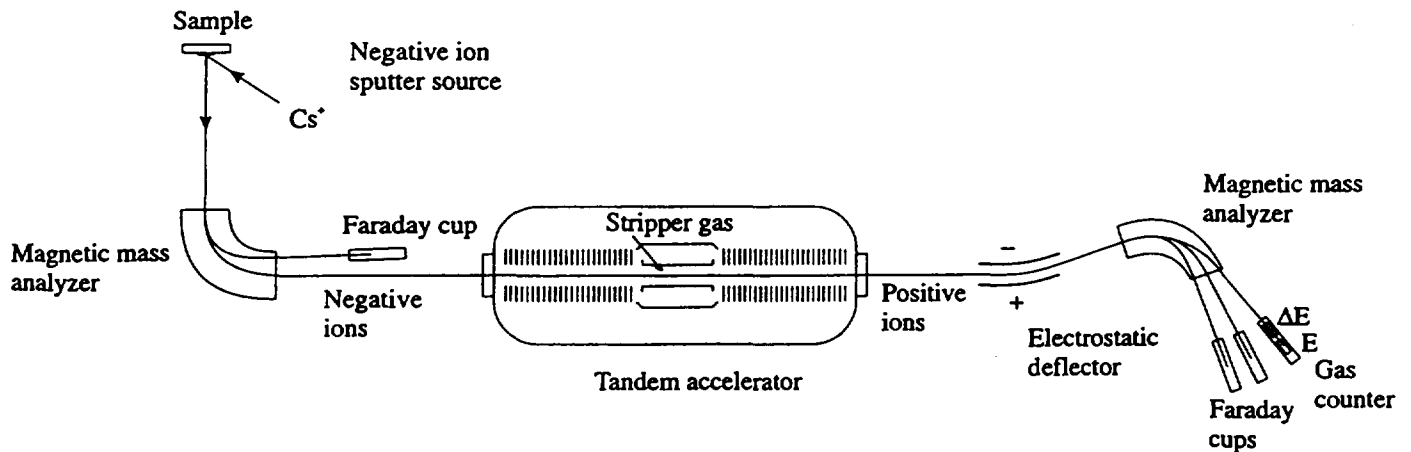


Figure 1.2: Schematic representation of an AMS-facility (from Finkel and Suter, 1993).

1.8 Outline of this work

In the first part of this work, the feasibility of dating ice cores by AMS with the cosmogenic nuclide ^{32}Si was investigated. Due to its low concentration in archives such as ice cores, a very large amount of material is needed to perform conventional activity measurements. The use of AMS should reduce the needed sample size. Therefore, $^{32}\text{Si}/\text{Si}_{\text{tot}}$ ratios in fresh snow from the Jungfrauoch were measured and compared to AMS background ratios.

The second part of this work is devoted to ^{36}Cl . Literature data show disagreement between measured and theoretical ^{36}Cl deposition rates. The theoretical calculations of the deposition rates are based on semi-empirical cross sections models, which could be inaccurate. The excitation function of the reaction $^{40}\text{Ar}(p,X)^{36}\text{Cl}$ was therefore measured and the experimental cross sections were used to model its atmospheric production and deposition rates.

2. ^{32}Si concentrations in fresh snow samples from the Jungfraujoch

High alpine glaciers are excellent archives of the air pollution history of central European countries. The analysis of ice cores from such glaciers allows the reconstruction of the atmospheric composition over more than 1000 years. The different layers of ice can be dated with ^3H or ^{210}Pb back to an age of 200 years, whereas ^{14}C is suitable for samples older than about 1000 years. Some natural events, such as volcanic eruptions, Saharan dust containing precipitation or forest fires give additional time horizons (Döscher, 1996). ^{32}Si , a cosmogenic radionuclide with a half-life of about 130 years (see chapter 2.2), is a potential new dating nuclide to cover the time gap between the above mentioned radionuclides.

^{32}Si is produced in the upper atmosphere by interaction of cosmic ray particles with argon, essentially through the neutron induced reaction $^{40}\text{Ar}(n, 3p6n)^{32}\text{Si}$. Its production rate is very low, about $1.6 \cdot 10^{-4} \text{ cm}^{-2}\text{s}^{-1}$, which is 10^4 times lower than the one of ^{14}C (Lal and Peters, 1967). ^{32}Si attaches rapidly to aerosol particle surfaces, and is removed from the atmosphere by wet or dry deposition.

^{32}Si could have a large range of applications in geoscience. Attempts were carried out to use it for groundwater dating (Fröhlich et al., 1988), in glaciology (Clausen, 1973), to study the deep-sea sedimentation (DeMaster and Cochran, 1982) and oceanic flow systems. The use of ^{32}Si as a tracer is however limited by its very small concentration in natural samples and by the high abundance of stable silicon in the lithosphere. In order to measure its concentration in precipitation by a classical activity determination, i.e. by β^- counting of its daughter ^{32}P , about one ton of material is needed. The use of AMS could reduce this huge amount of material. However, the present ^{32}Si chemical blanks for AMS correspond to an isotopic ratio of about 10^{-13} (Zimmermann and von Gunten, 1996). This value is still too high, since the present detection limit is $3.3 \cdot 10^{-15}$ (Zoppi et al., 1994), and the ratios found in natural samples below 10^{-14} (see Table 2.1).

Some long ice cores reaching bedrock were already drilled in the Alps (e.g. at the Colle Gnifetti, in the Monte Rosa massif). They were successfully dated and analyzed to an age of about 200 years (Döscher, 1996). To estimate the feasibility of dating such ice cores over about 1000 years, ^{32}Si activities and $^{32}\text{Si}/\text{Si}_{\text{tot}}$ ratios were measured in fresh snow samples of the Jungfraujoch in the Swiss Alps (3450 m. asl.).

However, the use of ^{32}Si to date ice cores is hampered by another problem: its production rate varies with the cosmic rays intensity, which is modulated by the 11 years cycle of the sun activity. This production rate variation, however, could be corrected using the ratio $^{32}\text{Si}/^{10}\text{Be}$, which should cancel the solar activity modulation. The use of the $^{32}\text{Si}/^{10}\text{Be}$ ratio is only possible if both nuclides

have an identical chemical behavior in the atmosphere, and if their production cross sections have about the same energy dependence. Both nuclides immediately attach to aerosol particles after formation, since they cannot form gaseous species. However, the excitation functions of the main reactions leading to atmospheric production of ^{10}Be and ^{32}Si , i.e., $^{14}\text{N}(n,2p3n)^{10}\text{Be}$, $^{16}\text{O}(n,3p4n)^{10}\text{Be}$ and $^{40}\text{Ar}(n,3p6n)^{32}\text{Si}$ are not well known, and their reaction thresholds are not identical (14.9 MeV, 31.9 MeV, and 15.8 MeV, respectively).

Table 2.1: $^{32}\text{Si}/\text{Si}_{\text{tot}}$ ratios in different aqueous samples.

Sample	$^{32}\text{Si}/\text{Si}_{\text{tot}}$
Rain water (Franke et al., 1986)	$1.3 \cdot 10^{-14} - 6.2 \cdot 10^{-16}$
River water (Lal and Somayajulu, 1984)	$1.5 \cdot 10^{-16} - 4.9 \cdot 10^{-17}$
Groundwater (Lal and Somayajulu, 1984)	$6.9 \cdot 10^{-17} - 9.8 \cdot 10^{-18}$
Ocean surface water (Lal and Somayajulu, 1984)	$9.7 \cdot 10^{-16} - 2.5 \cdot 10^{-16}$
Ice, Indian glacier (Nijampurkar et al., 1982)	$4.2 \cdot 10^{-15} - 4.8 \cdot 10^{-17}$

2.1 The half-life of ^{32}Si

The first half-life values reported in the literature for ^{32}Si covered a range between 80 and 700 years (Turkevich and Samuels, 1954; Geithof, 1962; Honda and Lal, 1964; Jantsch, 1967). More recent determinations were based on the measured decrease of the ^{32}Si concentration in dated ice or sediment cores. Several determinations used AMS by measuring the number of ^{32}Si atoms in samples of known activity, the activity being determined with liquid scintillation spectrometry of ^{32}P . The half-life of ^{32}Si was also determined by measuring its decay during four years. Finally, a recent work used the implantation of ^{32}Si high energy ions in a detector. Table 2.2 summarizes these more recent results.

The half-lives obtained from ice cores are by a factor of about two higher than the purely nuclear physical measurements. The mean value of the four AMS measurements is 126 years. The average value from the last 6 measurements listed in Table 2.2 is 135 years. This value will be used in this work.

Table 2.2: Most recent determinations of the half-life of ^{32}Si .

^{32}Si half-live [years]	Year of determination	Method	Reference
330±40	1973	Decrease with depth	Clausen, 1973
222,277	1980	Decrease with depth	DeMaster and Cochran, 1982
276±32	1980	Decrease with depth	DeMaster and Cochran, 1982
217±29	1983	Decrease with depth	Cumming, 1983
172±4	1986	Radioactive decay	Alburger et al., 1986
108±18	1980	AMS	Elmore et al., 1980
101±18	1980	AMS	Kutschera et al., 1980
133±9	1990	AMS	Hofmann et al., 1990
162±12	1991	AMS	Thomsen et al., 1991
132±12	1993	Implantation	Chen et al., 1993

2.2 Experimental

Four snow samples were collected in April 1993 and January 1994 at the Jungfraujoch (3450 m asl.), each sample corresponding to a mass of about one ton. The ^{32}Si , ^3H , ^7Be , ^{137}Cs , ^{210}Pb and Si_{tot} concentrations were measured in each sample.

The snow was collected at the tunnel exit of the Jungfraujoch, on the upper part of the Jungfrauim, and transported to the laboratory in plastic bags. There, the snow was melted in a heated metallic container and transferred into a 225±5 l cylindrical vessel. After melting, the sample was acidified with HCl to pH=3 to remove the carbonates, and 0.8 g Si (as $\text{Na}_2\text{SiO}_3 \cdot 9\text{H}_2\text{O}$) together with 72 g FeCl_3 were added. After stirring, the pH was increased to 9 with NH_4OH in order to precipitate $\text{Fe}(\text{OH})_3$. Then, a coagulation agent (Prestol) was added, and the solution was stirred and allowed to stand for 1 hour. After decanting the supernatant solution, the precipitate was collected in a plastic container. The operation was repeated until a total volume of water of about 1m³ was treated. The extraction of silica from the precipitate was carried out in Freiberg, Germany, after the method described by Gellerman et al. (1988). The efficiency for the silica recovery was about 90%. The final silica sample was stored for 3-5 months in order to reach the secular equilibrium between ^{32}Si and its daughter ^{32}P . After milking of ^{32}P in form of $\text{Mg}_2\text{P}_2\text{O}_7$, the activity was measured with a low level β^- counter, the properties of which are described in Table 2.3.

Table 2.3: Parameters of the ^{32}Si low level counter at Bergakademie Freiberg.

Background counting rate	B	3.56 ± 0.47	[cph]
Blank counting rate		4.62 ± 0.55	[cph]
Counting efficiency	η_D	0.627 ± 0.0007	
Figure of merit	$\eta_D/B^{0.5}$	0.295	[h ^{0.5}]
detection limit		0.1	[$\mu\text{Bq l}^{-1}$]

In order to obtain better statistics, the activities of the ^{32}P samples were measured several times so that a decay curve was obtained. The activity of ^{32}Si is then equal to the activity of ^{32}P at the time of milking.

The total silicon concentrations were determined with an ICP-OES apparatus after the following treatment: an aliquot of about 40 g snow was melted together with 1 g NaOH and dried in a silver crucible at 780°C for 10 min. The residual was dissolved in a H_2SO_4 solution, so that the final solution reached a pH of about 1.5 and a volume of 100 ml.

The tritium activities were measured by liquid scintillation spectrometry after preconcentration of the melted snow by electrolysis. An aliquot of the $\text{Fe}(\text{OH})_3$ precipitate was used for a γ -activity measurement of ^7Be and ^{137}Cs . The concentration of ^{10}Be was measured with the AMS facility in Zurich after preparing the target at EAWAG, Dübendorf (Beer et al., 1987). The ^{210}Pb activity was determined via the α -activity of its daughter ^{210}Po , which was deposited on silver disks (Gäggeler et al., 1983).

2.3 Results and discussion

Figure 2.1 depicts the decay measurements of the ^{32}P samples for the sample JFJ1 and JFJ2.

The four snow samples correspond to three different snowfall periods. JFJ1 and JFJ2 were collected on consecutive days. During the intermediate night, the snowfall became highly loaded with Saharan dust, indicated by the yellow - brown color of the snow. JFJ3 was divided into two independent samples, JFJ3a and JFJ3b. The particulate species contained in JFJ3b was coprecipitated without silicon carrier to test the method for a future AMS measurement of ^{32}Si in a snow sample. The results of the different nuclide concentrations measured in these four snow samples are summarized in Table 2.4.

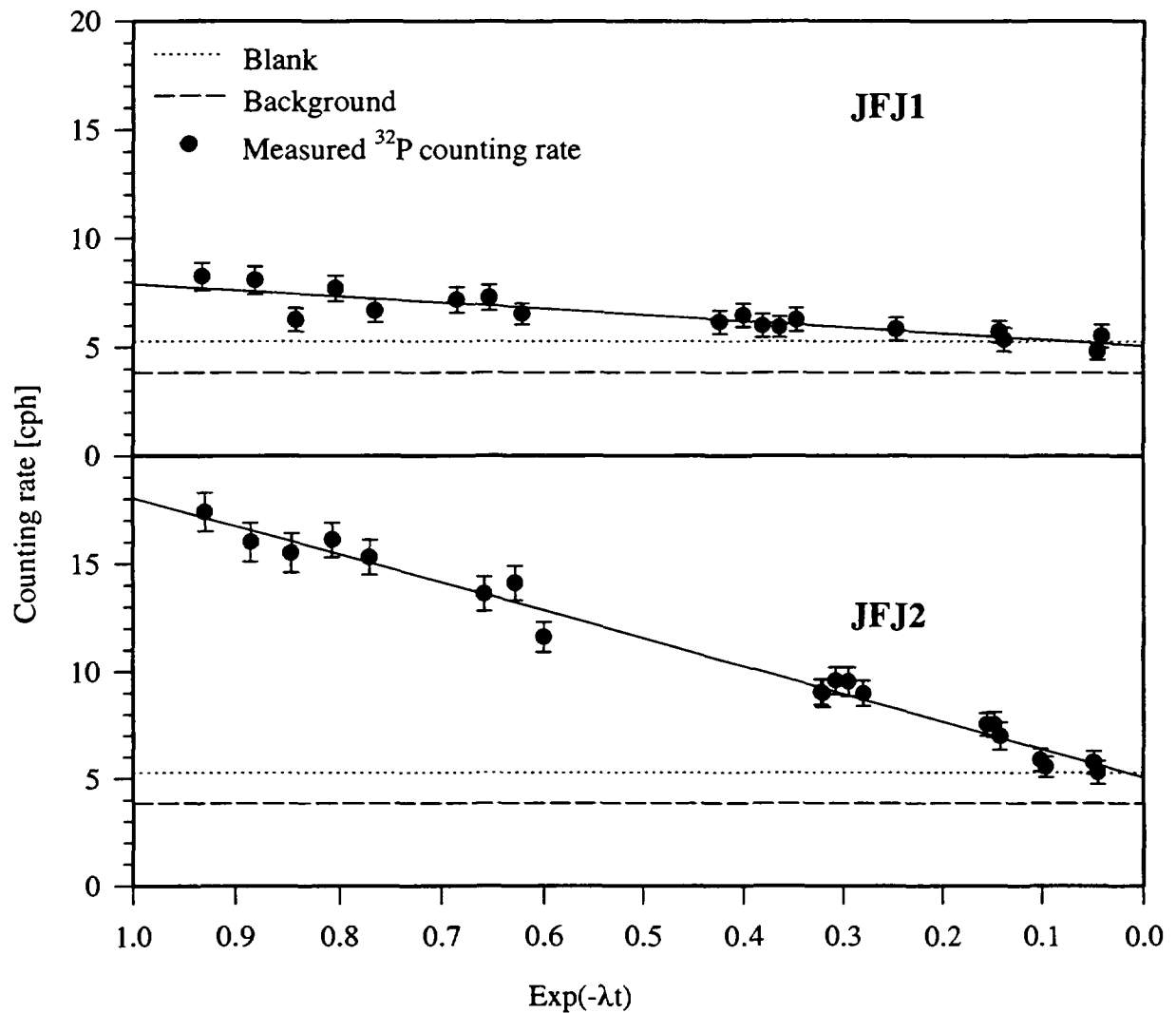


Figure 2.1: Decay measurements of ^{32}P samples. $\text{Exp}(-\lambda t)=1$, i.e. $t=0$ correspond to the time of milking.

The ^{32}Si activity concentrations are in good agreement with other values measured world-wide in precipitation samples (see figure 2.2). The sample JFJ2, which was contaminated with Saharan dust shows a significantly higher ^{32}Si concentration than the other samples, including JFJ1 which was collected one day before. This is probably due to an increase of the scavenging by the dust particles as shown by the increase of the ^7Be and ^{210}Pb activities. ^{210}Pb is a daughter product of the short-lived ^{222}Rn isotope ($T_{1/2} = 3.82$ days), which emanates from soils. An increase of the ^{210}Pb activity, as well as an increase of cations and anions were already recorded during another Saharan dust event at the Jungfraujoch (Schwikowski et al., 1995). The only nuclide which is not affected by the presence of Saharan dust is tritium, obviously because this nuclide is not scavenged by aerosol or dust particles.

Table 2.4: Results for the Jungfraujoeh snow samples.

Sample Snowfall	^{32}Si [$\mu\text{Bq/l}$]	Si_{tot} [mg/l]	$^{32}\text{Si}/\text{Si}_{\text{tot}}$	^7Be [Bq/l]	^{10}Be [10^6 at/l]	^{137}Cs [mBq/l]	^{210}Pb [mBq/l]	^3H [Bq/l]
JFJ1 26.4.1993	1.84 \pm 0.21	0.29 \pm 0.06	1.7 \cdot 10 $^{-15}$	0.57 \pm 0.03	¹	0.13 \pm 0.03	17.1 \pm 5.0	1.40 \pm 0.14
JFJ2 27.4.1993	6.28 \pm 0.40	70.6 \pm 1.7	2.5 \cdot 10 $^{-17}$	1.98 \pm 0.15	¹	0.99 \pm 0.08	1345 \pm 670	1.33 \pm 0.13
JFJ3a 16.1.1994	3.05 \pm 0.31	0.39 \pm 0.05	2.3 \cdot 10 $^{-15}$	1.07 \pm 0.11	9.68 \pm 1.9	0.20 \pm 0.02	78.1 \pm 19.6	0.80 \pm 0.09
JFJ3b 16.1.1994	2.87 \pm 0.34	²	²	1.03 \pm 0.10	²	0.30 \pm 0.03	²	²

¹ Measurement not carried out

² Same snow as sample JFJ 3a

Within experimental error, identical ^{32}Si activities were measured in the samples JFJ3a and JFJ3b, which shows that efficient ^{32}Si extraction may also be achieved without adding Si carrier. Thus, this extraction method is suitable for future AMS measurements of ^{32}Si concentrations in precipitation samples.

The $^{32}\text{Si}/\text{Si}_{\text{tot}}$ atomic ratios are between 1.7 \cdot 10 $^{-15}$ and 2.5 \cdot 10 $^{-17}$ which is by at least two orders of magnitude below the isotopic ratio of the AMS chemistry blanks. They are in good agreement with other measurements in precipitation samples or in ice (see Table 2.1).

The ^7Be concentrations are in good agreement with other values measured between 1993 and 1994 in rain samples from Switzerland which lie between 0.5 and 2 Bq/l (Surbeck and Ferreri, 1994) and with another mean value of 2.1 Bq/l measured in rain samples at about the same latitude in Illinois, U.S.A (Brown et al., 1989). These values are obviously higher than the 0.15 Bq/l measured in Antarctica (Nijampurkar and Rao, 1993), which is probably due to a latitude effect. The $^{32}\text{Si}/^7\text{Be}$ atomic ratio in the four Jungfraujoeh samples is constant and is about 3 \cdot 10 $^{-6}$. This is more than 20 times lower than the ratio measured in Antarctica (Nijampurkar and Rao, 1993), where an extremely high concentration of ^{32}Si was observed (see figure 2.2).

The ^{10}Be activity of sample JFJ3 is also in good agreement with the mean value of 11.5 \cdot 10 6 atoms/l measured at the Weissfluhjoeh in the Swiss Alps by Baltensperger et al. (1993). The $^7\text{Be}/^{10}\text{Be}$ atomic ratio of sample JFJ3 is 0.72, which agrees with the ratio of 0.68 measured in the Illinois State (Brown et al., 1989). The measured value of the $^{32}\text{Si}/^{10}\text{Be}$ atomic ratio, which is of great importance for dating purposes, is 1.9 \cdot 10 $^{-3}$. This value is lower by a factor of 2 than the theoretical value of 3.6 \cdot 10 $^{-3}$ calculated by Lal and Peters (1967) or the one of 3.4 \cdot 10 $^{-3}$ predicted by Oeschger et al. (1969).

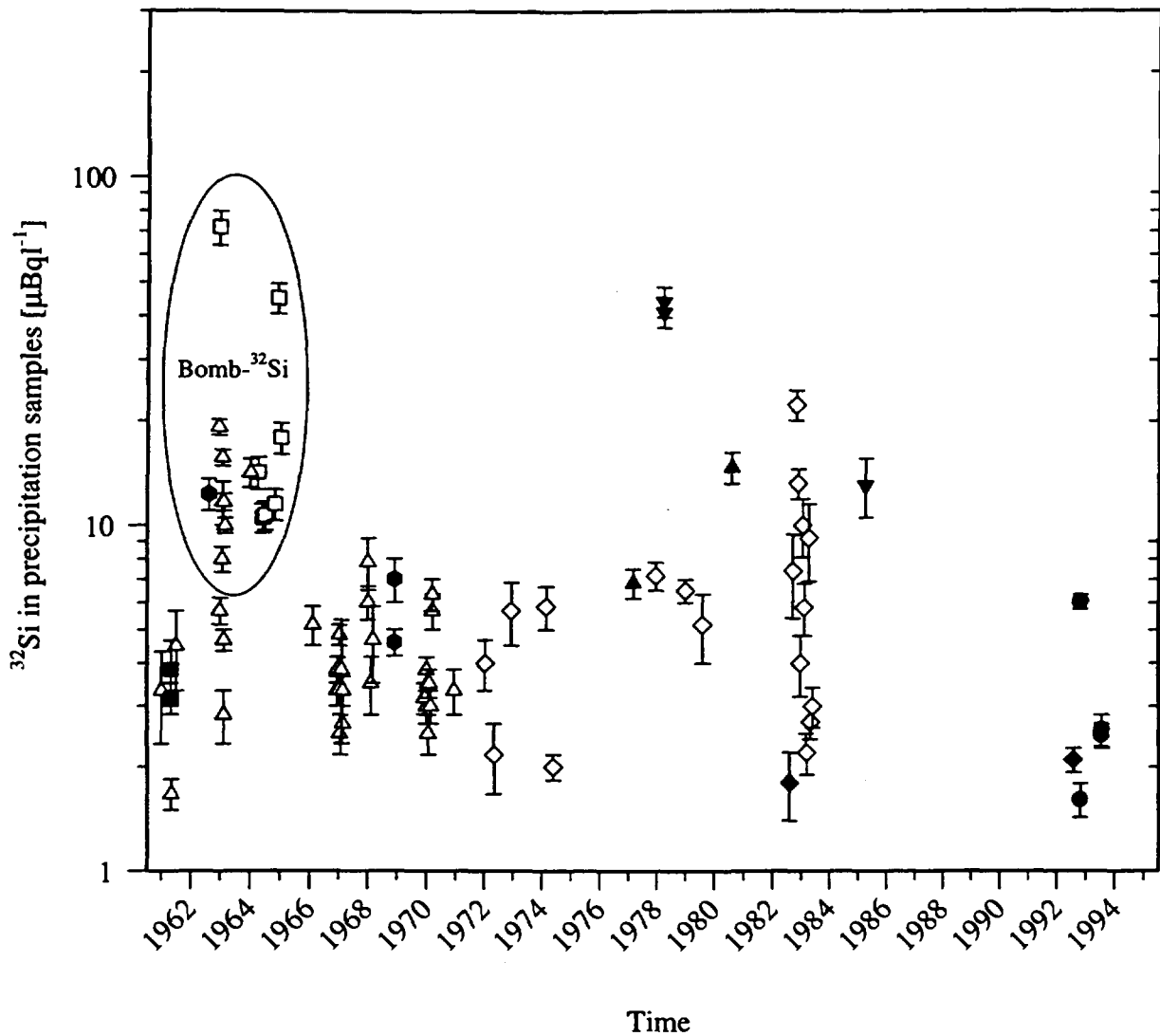


Figure 2.2: Worldwide concentrations of ^{32}Si in precipitation samples. Open symbols correspond to rain samples from Denmark (\square Dansgaard et al., 1966), India (\triangle Kharkar et al., 1966; Lal et al., 1979) and Germany (\diamond Franke et al., 1986). Full symbols correspond to snow samples from Denmark (\blacksquare Dansgaard et al., 1966), India (\blacktriangle Bandhari et al., 1981), Germany (\blacklozenge Franke et al., 1986; Morgenstern et al., 1996), Antarctica (\blacktriangledown Koch, 1982; Nijampurkar and Rao, 1993), Greenland (\bullet Clausen, 1973) and Switzerland (\bullet , this work). Evidence of ^{32}Si production during nuclear weapons tests is given by Dansgaard et al. (1966).

2.4 Conclusion

The concentrations of the different radionuclides measured in the three snow samples are generally in good agreement with other measurements in precipitation samples. The $^{32}\text{Si}/^7\text{Be}$ ratio was constant in all samples, including the sample containing Saharan dust, where a more efficient

scavenging of these radionuclides from the atmosphere was observed. This indicates that the $^{32}\text{Si}/^{10}\text{Be}$ ratio is probably also constant, which will allow its application for dating.

At present, AMS measurements of ^{32}Si concentrations in snow samples from the Alps are not possible. The chemistry blanks should reach about the same isotopic ratio as the AMS detection limit ($^{32}\text{Si}/\text{Si}_{\text{tot}} = 3.3 \cdot 10^{-15}$). In addition, efforts are being made to increase the sample ionization efficiency and the beam current of AMS to reduce the detection limit, so that AMS measurements of ^{32}Si concentrations in natural samples should be possible in the future. The present results show that the $\text{Fe}(\text{OH})_3$ coprecipitation method is also efficient without addition of silicon carrier, a prerequisite for an AMS measurement.

However, for accurate dating of glacier ice, the uncertainty in the half-life of ^{32}Si has also to be reduced.

3. Measurements of proton induced cross sections in gas targets

For many applications of cosmogenic isotopes, such as dating, knowledge of their input functions to the earth (i.e. their deposition rates) is mandatory. Many authors have published theoretical values for the production rates (Lal and Peters, 1967; Oeschger et al., 1969; O'Brien, 1979; Masarik and Reedy, 1995). The deposition rates can then be deduced using the tracer nuclide ^{90}Sr from the nuclear weapons testing. It is assumed that all cosmogenic nuclide behave similarly and that fallout does not depend on the latitude at which the nuclides were introduced in the stratosphere (Lal and Peters, 1967).

However, many measurements have shown that the theoretical production rate of ^{36}Cl in the atmosphere has been underestimated. For example, Synal et al. (1994) measured ^{36}Cl deposition rates in Greenland ice cores which are 2-5 times higher than estimated. To avoid the time dependence of the production rate of cosmogenic nuclides, attempts were carried out to date ice cores from Greenland using the $^{10}\text{Be}/^{36}\text{Cl}$ ratio (Suter et al., 1987; Elmore et al., 1987). These measured $^{10}\text{Be}/^{36}\text{Cl}$ ratios are lower than estimated ones (see Table 3.1), which also shows that the ^{36}Cl production rates have been underestimated, since theoretical and measured deposition rates of ^{10}Be are generally in good agreement.

Table 3.1: Comparison of theoretical and measured $^{10}\text{Be}/^{36}\text{Cl}$ ratios. The values in brackets are the calculated ^{10}Be and ^{36}Cl production rates in $\text{cm}^{-2}\text{s}^{-1}$.

$^{10}\text{Be}/^{36}\text{Cl}$	Determination	Reference
41 (4.5·10 ⁻² / 1.1·10 ⁻³)	Theoretical	Lal and Peters, 1967
29 (2.5·10 ⁻² / 8.7·10 ⁻⁴)	Theoretical	O'Brien, 1979
6.4 (1.4·10 ⁻² / 2.2·10 ⁻³)	Theoretical	Oeschger et al., 1969
17 (2.0·10 ⁻² / 1.2·10 ⁻³)	Theoretical	Masarik and Reedy, 1995
7.1	Weissfluhjoch, snow	Baltensperger et al., 1993
8.3	Camp-Century, Ice core	Elmore et al., 1987
6.5 - 9	Camp-Century, Ice core	Suter et al., 1987

The reaction cross sections used in the production rate calculations are based on semi-empirical models (Rudstam, 1966; Silberberg and Tsao, 1973), which may be inaccurate. Therefore, it is necessary to improve calculations on global production rates using experimental production cross sections. Although the secondary cosmic ray particle flux in the atmosphere consists mainly of

neutrons, the contribution of protons to radioisotope production has to be known. Moreover, the data obtained with protons allow to predict radioisotope production from the neutrons. Nevertheless, future experiments with monoenergetic, high energy neutron beams are required to obtain experimental excitation functions for (n,X) reactions.

In order to measure the excitation function of the reaction $^{40}\text{Ar}(p,X)^{36}\text{Cl}$, a gas target system was built. At present, no cross section data for irradiations of an argon target exist. However, measurements of excitation functions for other reactions of atmospheric importance (irradiation of oxygen and nitrogen) were already carried out (Bodemann et al., 1993). These cross sections were measured by irradiating solid binary compounds of nitrides and oxides, with the disadvantage that the nuclide of interest can also be produced from the other constituent of the compound. Thus, the excitation functions of the undesired reactions have to be known and subtracted.

3.1 The irradiation facilities

The gas target irradiations were carried out at two different facilities of the Paul Scherrer Institute: The Proton Irradiation Facility (PIF) and the Philips Cyclotron (PC).

The proton beam for the PIF is delivered by a parasitic beam of the 590 MeV ring accelerator. It passes through a permanent copper-graphite degrader to reach an energy of 300 MeV. The current is limited to about 3 nA to avoid air activation in the experimental area. 590 MeV irradiations are only possible if the copper-graphite degrader is removed from the beam line. Behind the beam pipe, the protons pass through a set of collimators, ionization chambers and aluminum degraders (see figure 3.1) prior to the target. Irradiations are carried out in air.

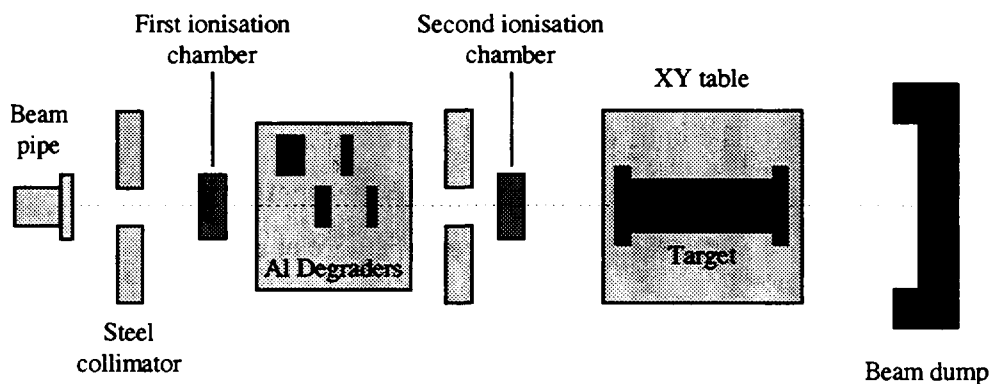


Figure 3.1: Schematic representation of the PIF experimental setup.

The irradiation energy is chosen via appropriate choice of the thickness of the aluminum degrader set. This leads to an increase of the energy resolution with decreasing energy. Our targets were therefore irradiated at the PIF with a minimum energy of 40 MeV, because the energy resolution was too large for lower energies.

In the 10-50 MeV energy range, the targets were irradiated at the Philips Cyclotron. The PC is an energy variable cyclotron, so that no degradation of the beam is necessary. It can provide a proton beam up to 72 MeV, with a maximum current of about 100 μA . Since we carried out the irradiations in air, we have only a current of 50 nA to avoid a significant activation in the experimental area. The schematic setup of the experiment is shown in figure 3.2.

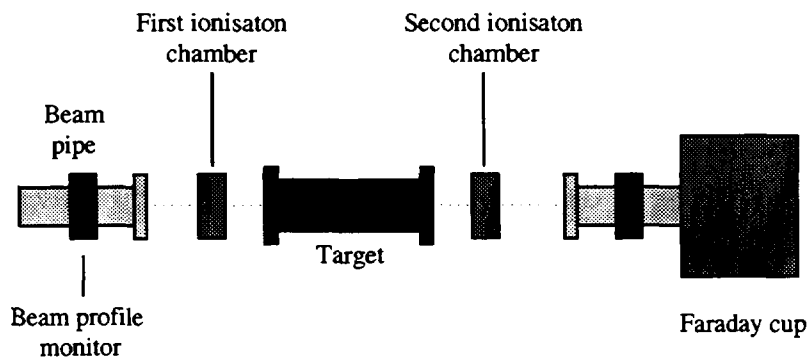


Figure 3.2: Schematic representation of the PC experimental setup.

3.2 The gas target

The gas target consists of a steel cylinder (length = 34.4 cm, diameter = 15.3 cm) tightly closed at both ends with aluminum windows, with the thicknesses adjusted according to the inner gas pressure (0.3 mm for 1 bar and 0.5 mm for 3 bar). Pure argon and nitrogen gases were used for PIF irradiations, whereas the targets were filled with a mixture of 5% nitrogen in argon for PC irradiations. The inner surface of the tube was covered with a 17 μm thick aluminum foil to collect the produced nuclides by surface adsorption. Before filling, the gases were filtered through an aerosol filter. The exact quantity of gas was determined by weighing.

To obtain enough ^{36}Cl and ^{10}Be atoms for an AMS measurement, one hour for ^{36}Cl production and 12 hours for ^7Be and ^{10}Be were necessary at the PIF, whereas about one hour was sufficient to produce ^{36}Cl , ^7Be and ^{10}Be at the PC.

Table 3.2: Summary of performed irradiations.

Sample series	Facility	Gases, pressure	Produced nuclides	#Runs/#Energies	Bombarding time
WQCL	PIF	Ar, 3 bar	^{36}Cl	17/9	1 hour
WQCL'	PC	5% N_2 in Ar, 1 bar	^{36}Cl , ^{10}Be , ^7Be	10/5	1 hour
WQBE	PIF	N_2 , 3 bar	^7Be , ^{10}Be	2/2	12 hours

3.3 The proton dose measurements

For cross section measurements, special care of the proton flux measurements has to be taken. The most used monitoring method is the activation of an aluminum foil placed in the beam line. The production of ^{22}Na in this foil allows to calculate the number of protons which passed through it, the excitation function of the $^{27}\text{Al}(p,3p3n)^{22}\text{Na}$ being very well known (Stein et al., 1990; Tobailem et al., 1981).

The Proton Irradiation Facility has additional equipment to measure proton doses. Two ionization chambers which were calibrated with a plastic scintillator, are placed in the beam line (see figure 3.1). Since the proton doses applied to the target were not high enough to produce a detectable activity of ^{22}Na , some cross sections were measured by irradiation of solid nickel targets. The comparison of these cross sections with literature data allows to test the accuracy of the ionization chambers. The number of protons measured with the ionization chambers during the PIF irradiations are summarised in Table 3.3.

These ionization chambers were also placed in the beam line during the PC irradiations. However, due to the higher current used during these bombardments, the count rates were saturated, and other techniques had to be used. It was also impossible to use a Faraday cup, due to the high divergence of the beam at low energies caused by straggling, as shown by the beam profile monitor placed in front of the Faraday cup (see figure 3.2). The Faraday cup has however been used indirectly. First, we used a Monte-Carlo simulation to calculate the percentage of the protons which did not enter the Faraday cup. Second, the ratio of the Faraday cup to the ionization chamber signal was measured during a calibration experiment. This calibration allowed to determine the number of protons which did not enter the Faraday cup. The activation of aluminum was used only for the three highest energies of the PC irradiations, since the two lowest ones were below the threshold energy of the reaction $\text{Al}(p,3p3n)^{22}\text{Na}$.

Table 3.3: Number of protons measured during PIF irradiations.

Sample	Al-degrader thickness [mm]	Energy [MeV]	Number of protons [10^{12}]
WQCL 1	205	94.7 ± 4.4	3.04 ± 0.16
WQCL 2	0	292.2 ± 1.2	3.13 ± 0.16
WQCL 3	119	188.5 ± 3.0	2.96 ± 0.15
WQCL 4	119	188.5 ± 3.0	2.95 ± 0.15
WQCL 5	167	141.2 ± 3.4	2.96 ± 0.15
WQCL 6	187	118.2 ± 3.8	2.98 ± 0.15
WQCL 7	231	46.7 ± 7.8	2.90 ± 0.15
WQCL 8	226	60.4 ± 5.9	3.55 ± 0.18
WQCL 9	216	77.2 ± 5.1	3.08 ± 0.16
WQCL 10	216	77.2 ± 5.1	3.09 ± 0.16
WQCL 11	231	46.7 ± 7.8	2.93 ± 0.15
WQCL 13	226	60.4 ± 5.9	3.58 ± 0.18
WQCL 14	0	587.9 ± 0.4	5.00 ± 0.26
WQCL 15	0	587.9 ± 0.4	11.3 ± 0.60
WQCL 16	0	302.2 ± 1.1	3.81 ± 0.19
WQCL 17	119	188.8 ± 2.8	3.00 ± 0.15
WQBE 1	0	588.0 ± 0.3	99.6 ± 5.08
WQBE 2	0	302.3 ± 1.1	20.0 ± 1.02

The following chapters give more detailed information on the monitoring methods used during the PC irradiations. The results for nickel cross sections measured during the PIF irradiations will be presented in chapter 3.5.

3.3.1 Monitoring using a Monte-Carlo simulation

We used a computer program (Geant Code, 1993) which performs a Monte-Carlo simulation in order to calculate the energy, beam and radial profiles of the protons at the desired places of our experimental setup. The precise geometry of the experimental setup and the following initial conditions were entered into the program:

1. 10^7 protons are generated in the beam pipe.
2. The energy spectrum in the beam pipe is a δ -function.
3. The beam profile in the beam pipe is a three dimensional gaussian like shape with $\sigma(x) = \sigma(y) = 4$ mm.

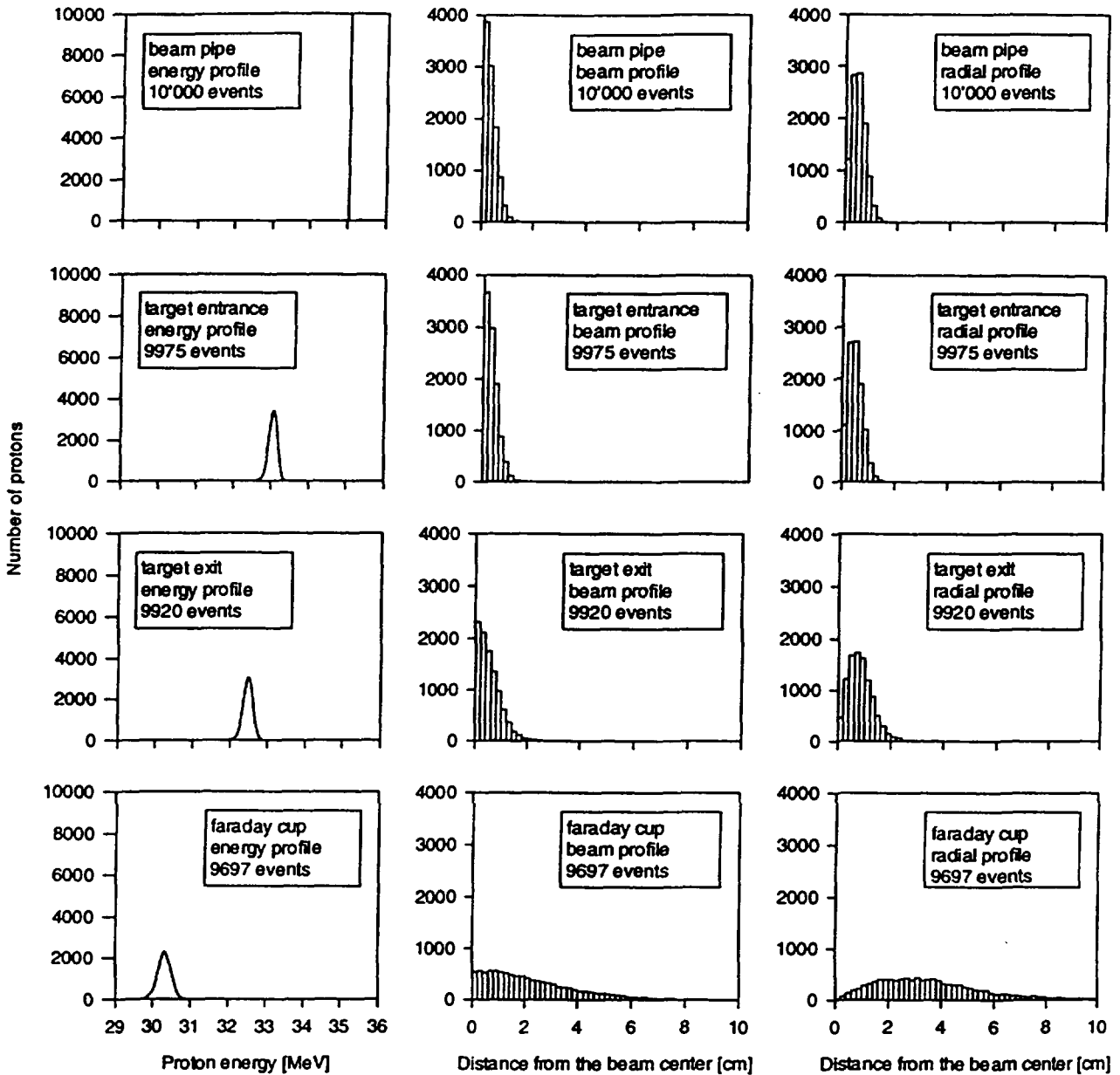


Figure 3.3: Results of the Monte-Carlo simulation for $E_0 = 35.03$ MeV. The beam and radial profiles calculation steps correspond to 0.2 cm, whereas the energy profile steps are about 0.1 MeV.

These initial conditions are only an approximation of the real conditions. In fact, the targets were irradiated with a total of about 10^{15} protons, the energy spectrum in the beam pipe was gaussian with $\sigma \cong 0.2$ MeV. The beam profiles, which are the most important parameter for our purpose, were well approximated: gaussian shapes with $2 \text{ mm} < \sigma(x)$ and $\sigma(y) < 6 \text{ mm}$ were measured by the first beam profile monitor. Results of the Monte-Carlo simulation carried out for the initial energy of 35.03 MeV are shown in figure 3.3.

As shown in figure 3.3, all protons crossed the target, since the target radius was larger than the beam profile at the target exit. In contrast, the Faraday cup radius was smaller than the beam profile at this point. The radial profile shows that 20 % of the protons were not counted by the Faraday cup which had a radius of only 5 cm. The radial profile is the first derivative of the beam profile and corresponds to the number of protons localized in a ring of width Δr (areal density). This allows to correct the number of proton measured in the Faraday cup to the number of protons which crossed the target:

$$\frac{N_p(mes)}{N_p(real)} = \frac{\sum_0^{5cm} R_{FC}(r)\Delta r}{\sum R_T(r)\Delta r} \quad (3.1)$$

Where: $N_p(mes)$: Number of protons measured in the Faraday cup

$N_p(real)$: Number of protons which crossed the target

$R_{FC}(r)$: Radial profile at the Faraday cup

$R_T(r)$: Mean of both radial profiles at the target entrance and exit

This method was used for the four highest PC irradiation energies. For the lowest energy, the experimental setup was changed in order to avoid a too high beam divergence. In this case, the first beam profile monitor was removed, the target was shifted as close as possible to the beam pipe, and the Faraday cup was moved directly behind the target.

3.3.2 Monitoring with Faraday cup - ionization chamber calibration curves

Measurements of the ionization chambers counting rate reached saturation for beam currents above about 10 nA, i.e. the function was linear only in the 1-10 nA range. However, we have measured the ionization chamber counting rate as a function of the Faraday cup counting rate without target in the beam current range from 20 to 100 nA. If all protons entered the Faraday cup, this function can be used as a calibration curve. In two cases, this condition was fulfilled: at the highest energy (61.05 MeV in the beam pipe), where the divergence was small enough, and at the lowest energy (16.90 MeV in the beam pipe), since the calibration curve was measured by shifting the Faraday cup as close as possible to the ionization chamber. In the range of the ionization chamber counting rate at which the targets were irradiated (250-600 s⁻¹), the following approximation was used (see figure 3.4, left):

$$C_{FC} = a(E) \cdot C_{IC} + b(E) \quad (3.2)$$

Where: C_{FC} : Counting rate of the Faraday cup [s^{-1}], with $1 s^{-1} \equiv 10 nA$

C_{IC} : Counting rate of the ionization chamber [s^{-1}]

$a(E)$ and $b(E)$: Regression factors

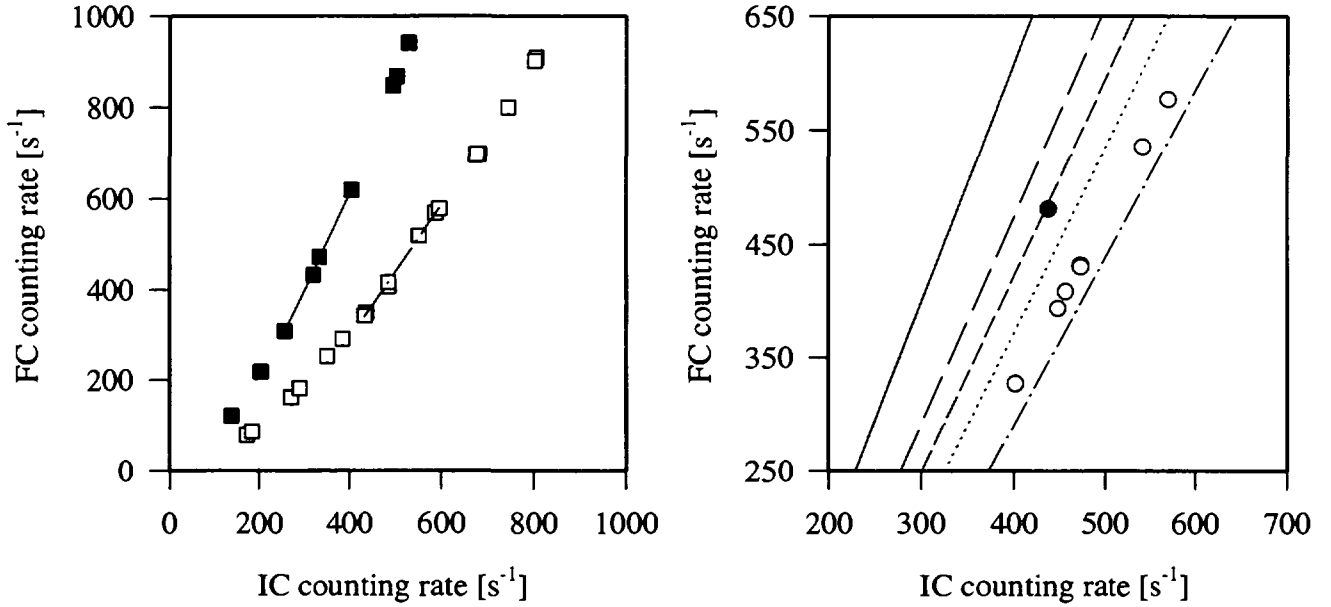


Figure 3.4: Left: Faraday cup counting rate as a function of ionization chamber counting rate. The linear range indicated by the solid lines corresponds to the ionization chamber counting rate at which the target irradiations were performed. ■: $E_{IC} = 60.73$ MeV, □: $E_{IC} = 16.19$ MeV, where E_{IC} is the energy in the middle of the ionization chamber. Right: Calculated calibration curves compared to some measured values. ●: $E_{IC} = 34.52$ MeV, ○: $E_{IC} = 27.50$ MeV. From left to right, the lines correspond to the following decreasing energies: $E_{IC} = 60.73, 41.86, 34.52, 27.50$ and 16.19 MeV.

Supposed that the factors $a(E)$ and $b(E)$ depend linearly on the energy, they can be calculated as a function of the energy in the ionization chamber from the two calibration energies, 60.73 MeV and 16.19 MeV, via:

$$a(E) = 0.01417 \cdot E_{IC} + 1.241 \quad (3.3)$$

and:

$$b(E) = 1.4634 \cdot E_{IC} - 321.11 \quad (3.4)$$

Where: E_{IC} : Energy in the ionization chamber [MeV]

These calculated calibration curves are compared to measured values in figure 3.4 (right). For $E_{IC} = 34.52$ MeV, the measured value agrees well with the calculated curve. On the other hand, all measured values at $E_{IC} = 27.50$ MeV deviate by about 13% from the calculated curve, showing that 13% of the protons have not entered the Faraday cup.

When placing a target in the beam line, the divergence was larger, and an additional part of the protons did not reach the Faraday cup. For each target irradiation, we calculated the true Faraday cup counting rate from the first ionization chamber counting rate, using eq. 3.2. The Faraday cup counting rate had to be further corrected for a zero current of about 0.18 nA.

The number of protons which crossed the target is then given by eq. 3.5:

$$N_p = 6.23 \cdot 10^9 \cdot I_{FC} \cdot t_{irr} \quad (3.5)$$

Where: N_p : Number of protons

t_{irr} : Irradiation time [s]

The counting rates of the ionization chambers as well as of the Faraday cup were recorded on line by a computer. Unfortunately, it was impossible to start or to stop an irradiation directly from this computer. We always started the counting program slightly before an irradiation and stopped it after the end of the bombardment. This resulted in a small overestimation of the irradiation time and an according underestimation of the ionization chamber counting rate. In order to take this into account, the recorded beam time was reduced by 120 s and the ionization chamber counting rate corrected accordingly. However, the major contribution to the error on the number of protons was due to the error of the factors $a(E)$ and $b(E)$.

3.3.3 Monitoring with the reaction $^{27}\text{Al}(p,3p3n)^{22}\text{Na}$

Since the target cylinders were closed at both sides with aluminum windows, we used those windows for a measurement of the ^{22}Na activity. Due to the energy loss, the proton energy in the first window was higher than in the second one. After bombardment, we discriminated the windows placed at the target entrance and at the exit by autoradiography. The image appearing on the film was smaller and more intense for the entrance window than for the second window, due to the straggling of the beam. Moreover, this procedure allowed to determine the center of the beam.

We placed then each window at a distance of 15 cm from a Germanium detector in order to minimize geometrical effects due to the size difference between the activity spots on the windows

and a calibration source, and measured the ^{22}Na activity via its 1275-keV γ -line. From this activity the proton dose was calculated using the following equation:

$$A_i = \Phi_p \cdot N_T \cdot \sigma_{i,T}(E) \cdot x_T \cdot (1 - e^{-\lambda_i \cdot t_{irr}}) \quad (3.6)$$

Where: A_i : Activity of the produced nuclide i [Bq]

Φ_p : Proton flux [s^{-1}]

N_T : Atomic density of the target [cm^{-3}]

$\sigma_{i,T}(E)$: Cross section for the reaction $T(p,X)i$ [cm^2]

x_T : Target thickness [cm]

λ_i : Decay constant of the nuclide i [s^{-1}]

t_{irr} : Irradiation time [s]

Knowing that:

$$\lim_{\lambda \rightarrow 0} \left[\frac{(1 - e^{-\lambda \cdot t_{irr}})}{\lambda} \right] = t_{irr} \quad (3.7)$$

and that, for our irradiation conditions, eq. 3.7 is valid for ^{22}Na ($\lambda = 8.45 \cdot 10^{-9}$ s), we can write:

$$N_{^{22}\text{Na}} = \frac{A_{^{22}\text{Na}}}{\lambda_{^{22}\text{Na}}} = \Phi_p \cdot N_{\text{Al}} \cdot \sigma_{^{22}\text{Na,Al}}(E) \cdot x_{\text{Al}} \cdot t_{irr} = N_p \cdot N_{\text{Al}} \cdot \sigma_{^{22}\text{Na,Al}}(E) \cdot x_{\text{Al}} \quad (3.8)$$

Where: $N_p = \Phi_p \cdot t_{irr}$: Number of protons which crossed the target

In addition, for our 0.3 mm thick windows, the energy loss cannot be neglected for energy ranges where the excitation function is not constant. For the reaction $^{27}\text{Al}(p,3p3n)^{22}\text{Na}$, this is the case between 30 and 70 MeV. Eq. 3.8 has then to be differentiated:

$$dN_{^{22}\text{Na}} = N_p \cdot N_{\text{Al}} \cdot \sigma_{^{22}\text{Na,Al}}(E(x)) \cdot dx_{\text{Al}} \quad (3.9)$$

In order to integrate eq. 3.9 over the window thickness, it is necessary to express the cross section as a function of the target thickness. The thickness of the window was small enough so that the energy dependence was assumed to be:

$$E(x_T) = E_0 - k(E_0) \cdot x_T \quad (3.10)$$

Where: $E(x_T)$: Energy at a depth x_T [MeV]

E_0 : Energy in front of the window [MeV]

$k(E_0)$: Constant depending on the initial energy [$\text{MeV} \cdot \text{cm}^{-1}$], calculated using the tables of Ziegler *et al.* (1988).

The excitation function of the reaction $^{27}\text{Al}(p,3p3n)^{22}\text{Na}$ has been extensively studied by many authors. Since the published values show large discrepancies, Tobailem *et al.* (1981) presented a set of recommended cross section values to be used for monitoring purposes. Steyn *et al.* (1990) measured very thoroughly the excitation function in the 25-200 MeV proton energy range. These data are in very good agreement with the recommended values of Tobailem *et al.* (1981). We used the excitation function of Steyn *et al.* (1990) (see figure 3.5), since it contains the largest number of values in the energy range of interest for our experiment.

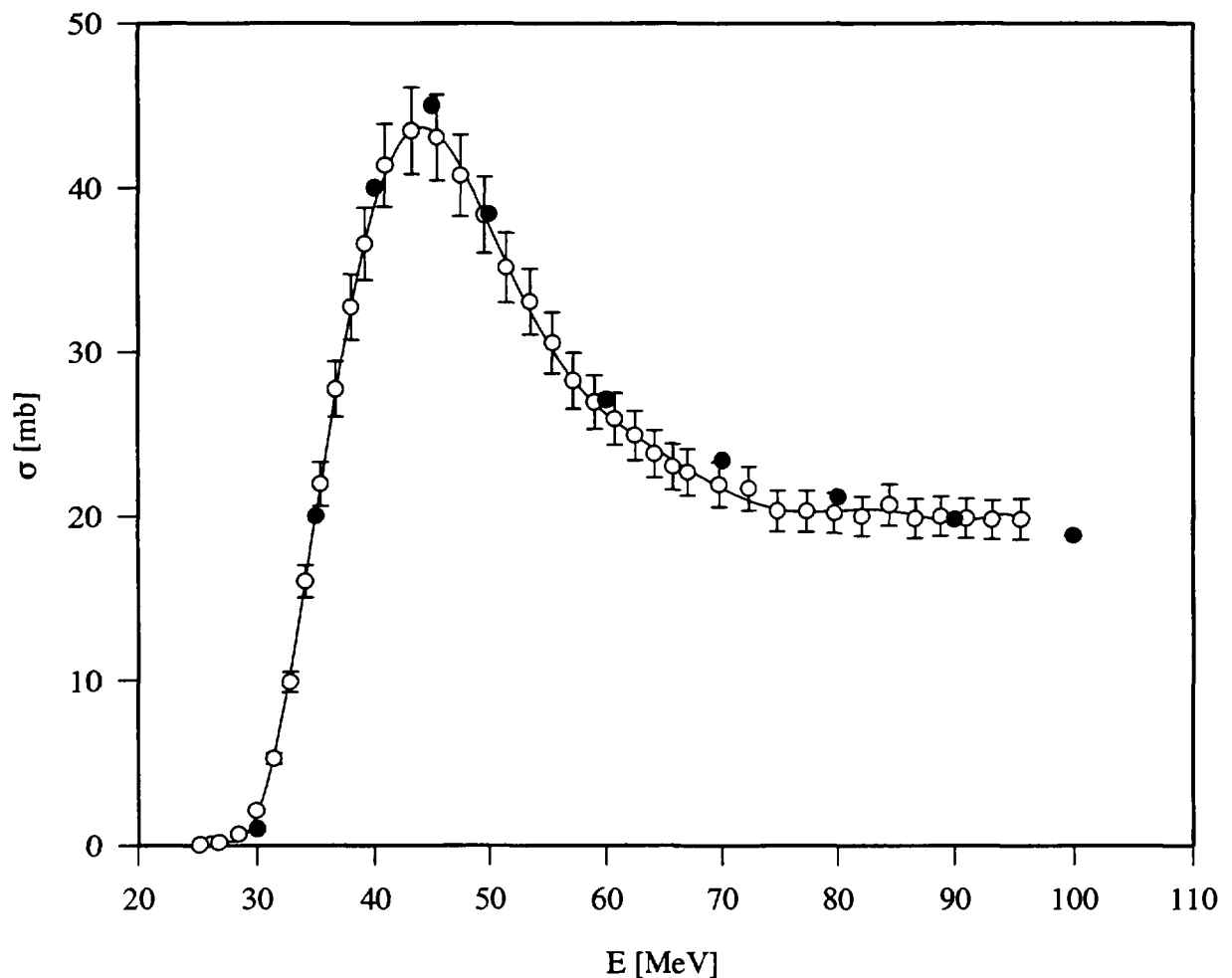


Figure 3.5: Cross sections of the reaction $^{27}\text{Al}(p,3p3n)^{22}\text{Na}$. Open symbols are the measured values of Steyn *et al.* (1990) fitted with a 10^{th} order polynomial, whereas the filled symbols are the recommended values of Tobailem *et al.* (1981).

In order to facilitate the integration of eq. 3.9, we fitted the excitation function with a 10th order polynomial so that the cross section could be expressed as a function of the window thickness:

$$\sigma_{^{22}\text{Na}}(x_{\text{Al}}) = a_0 + a_1 \cdot (E_0 - k(E_0) \cdot x_{\text{Al}}) + \dots + a_{10} \cdot (E_0 - k(E_0) \cdot x_{\text{Al}})^{10} \quad (3.11)$$

Where: a_0, \dots, a_{10} : polynomial factors

Equation 3.9 can now be integrated by substituting $\sigma_{^{22}\text{Na}}(x_{\text{Al}})$ with eq. 3.11:

$$N_{^{22}\text{Na}} = N_p \cdot N_{\text{Al}} \cdot \int_0^{0.3\text{mm}} \sigma_{^{22}\text{Na}}(x_{\text{Al}}) \cdot dx_{\text{Al}} \quad (3.12)$$

This method is applicable only for proton energies higher than about 30 MeV (see figure 3.5).

For each target, the ²²Na activities of both windows were measured. The number of protons was then calculated taking into account the different initial energies at the entrance of both windows. The differences of the obtained proton doses were always smaller than 4%, which is below other experimental errors. Moreover, we checked the consequence of an inaccurate centering of the window in front of the germanium detector. A 2 cm horizontal shift of the beam spot center with respect to that of the detector gave no change of the counting rate.

3.3.4 Comparison of the results

Table 3.4: Comparison of the measured number of protons with three different techniques.

Sample	Energy [MeV]	Number of protons [10^{15}]			
		Monte-Carlo simulation	Calibration curves	Aluminum activation	Weighted mean
WQCL' 1	59.62 ± 0.41	1.38 ± 0.12	1.19 ± 0.13	1.27 ± 0.06	1.28 ± 0.05
WQCL' 2	59.62 ± 0.41	1.68 ± 0.12	1.35 ± 0.17	1.49 ± 0.07	1.52 ± 0.06
WQCL' 4	40.36 ± 0.48	2.09 ± 0.16	1.90 ± 0.19	2.04 ± 0.11	2.03 ± 0.08
WQCL' 5	40.36 ± 0.48	1.52 ± 0.13	1.34 ± 0.15	1.57 ± 0.09	1.52 ± 0.07
WQCL' 6	32.76 ± 0.53	1.68 ± 0.16	1.69 ± 0.15	1.62 ± 0.21	1.67 ± 0.10
WQCL' 7	32.76 ± 0.53	1.62 ± 0.16	1.57 ± 0.15	1.62 ± 0.21	1.60 ± 0.09
WQCL' 8	25.39 ± 0.60	1.38 ± 0.13	1.44 ± 0.18		1.40 ± 0.10
WQCL' 9	25.39 ± 0.60	1.25 ± 0.12	1.33 ± 0.18		1.27 ± 0.10
WQCL' 10	12.91 ± 0.82		1.98 ± 0.16		1.98 ± 0.16
WQCL' 11	12.91 ± 0.82		1.43 ± 0.13		1.43 ± 0.13

The results obtained with the three different methods are summarized in Table 3.4. The given numbers of protons measured with the activation method is the mean from both windows. For all samples, and within error, the three different methods show good agreement (see figure 3.6).

To calculate the reaction cross sections, a weighted mean of the three values was used.

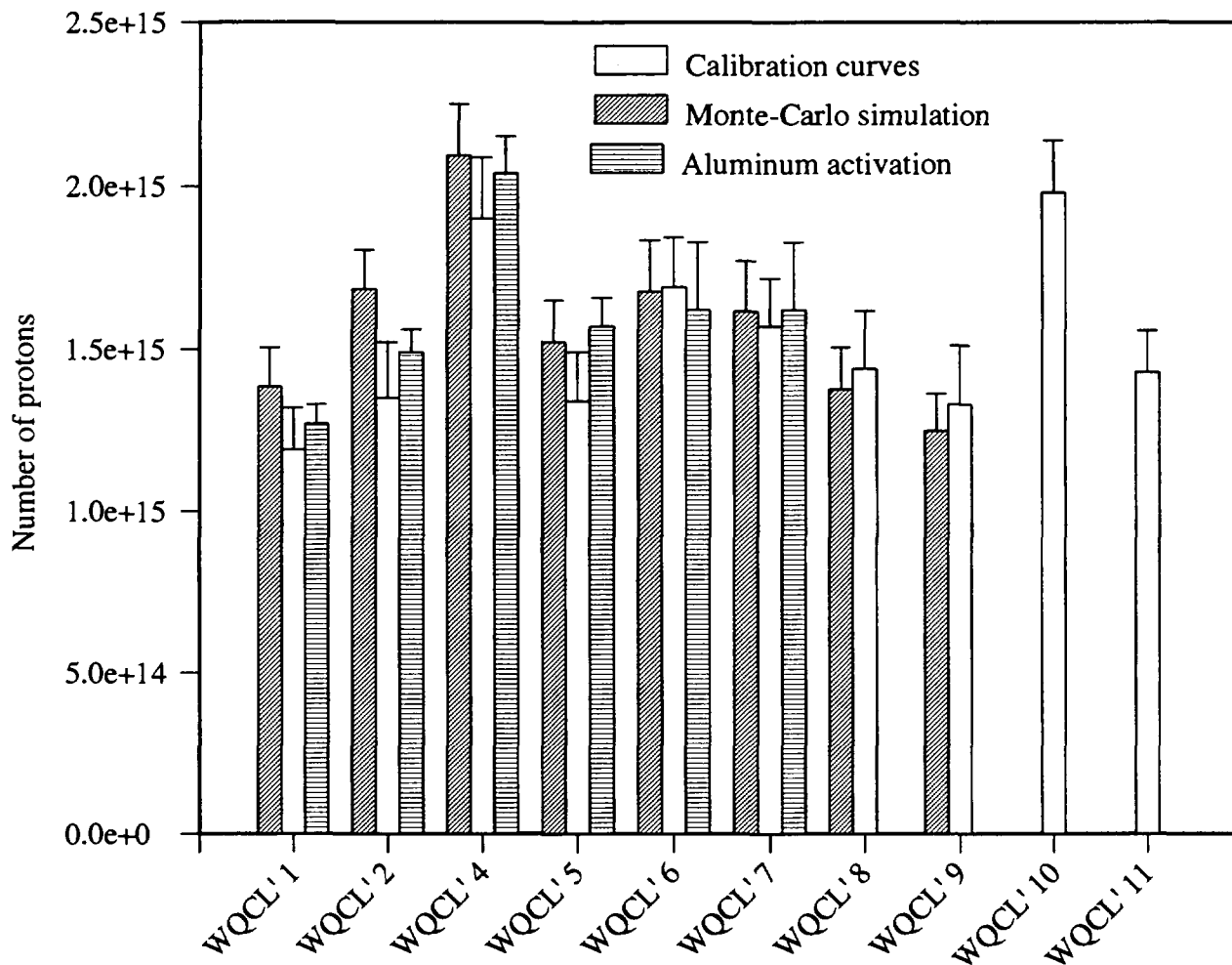


Figure 3.6: Comparison of the measured number of protons using three different techniques.

3.4 Treatment of the targets after irradiation

After irradiation, the target cylinders were evacuated through a glass fibre filter, which was first immersed in a 2% NaOH solution and dried, in order to collect nuclides that were not adsorbed on the aluminum foil, either due to attachment to residual aerosol particles in the gas or due to formation of gaseous acidic compounds.

Then, the filter was immersed into a NaCl-BeSO₄ carrier solution and put in an ultrasonic bath for 30 min at 30°C. The solution was filtered and transferred to a 10% NaOH solution, which also

contained Cl^- and Be^{2+} carriers, so that the total amount of carrier was about 20 mg Cl and 60 mg Be, respectively. The aluminum windows were immersed in this solution for 10 min in order to dissolve the surface layers. The 17- μm thick aluminum foil from the sidewalls was completely dissolved in the same solution. After filtration, the pH of the solution was adjusted to 7 by addition of concentrated HNO_3 , which resulted in a precipitation of $\text{Al}(\text{OH})_3$ and $\text{Be}(\text{OH})_2$. The precipitation was centrifuged, decanted and rinsed twice with water. AgNO_3 was added to the liquid phase in order to precipitate AgCl , which was separated by centrifugation and dissolved in a small amount of NH_4OH . In order to eliminate the isobaric nuclide ^{36}S from ^{36}Cl , BaSO_4 was precipitated by addition of $\text{Ba}(\text{NO}_3)_2$. After filtration, AgCl was precipitated again by addition of HNO_3 , separated by centrifugation, rinsed twice with water and dried. About 60% of the added chlorine carrier was recovered. The ratio $^{36}\text{Cl}/\text{Cl}$ was measured with the PSI-ETH AMS facility at Zurich-Hönggerberg.

The $\text{Al}(\text{OH})_3$ and $\text{Be}(\text{OH})_2$ precipitations were redissolved in a 20% HCl solution and introduced into a 1 litre polyethylene bottle. In the case of pure nitrogen irradiations, the aluminum foil and windows were directly dissolved in a 20% HCl solution, since no ^{36}Cl is formed with nitrogen. The beryllium carrier concentration was measured with inductively coupled plasma - optical emission spectroscopy (ICP-OES), showing a 95-100% recovery yield. The ^7Be activity was measured in the polyethylene bottle with γ -spectroscopy via its 477.6-keV line. Based on published cross sections (Bodemann et al., 1993), the production of ^7Be in the aluminum windows can be neglected ($\leq 1\%$ relative to the production in nitrogen).

Beryllium was then separated from aluminum with an adaptation of the procedure described by Baker et al. (1958), because a simple ion exchange chromatography was not possible due to a too large amount of aluminum in the sample. The beryllium solution was reduced to about 200 ml by evaporation. 100 ml ether were added, the solution was cooled in an ice bath and saturated with gaseous HCl to precipitate AlCl_3 . BeCl_2 does not precipitate under these conditions, since it is complexed by ether. The solution was then filtered and reduced to a small volume by evaporation. NH_4OH was added to precipitate $\text{Be}(\text{OH})_2$. The precipitate was centrifuged and the supernatant solution decanted. $\text{Be}(\text{OH})_2$ was redissolved in glacial acetic acid and the solution evaporated to dryness. This operation was repeated three times in order to form basic beryllium acetate ($\text{Be}_4\text{O}(\text{C}_2\text{H}_3\text{O}_2)_6$). The final basic beryllium acetate was dissolved in CHCl_3 and washed three times with water. The CHCl_3 solution was evaporated to near dryness, then, conc. HNO_3 was added, and again evaporated to dryness. The solid was redissolved in water, and $\text{Be}(\text{OH})_2$ was precipitated by addition of NH_4OH , separated by centrifugation and washed two times with water. In order to eliminate the last traces of aluminum, the hydroxide was redissolved in a 0.5M HCl solution and eluted on a DOWEX 50W (200-400 mesh) cation exchange chromatography column with 1M HCl

to separate Be. Under these conditions, Al remains on the column. $\text{Be}(\text{OH})_2$ was precipitated again, centrifuged, rinsed three times with water and dried. It was then introduced in a quartz crucible and heated at 1000°C during one hour in air to form BeO. The overall yield for this entire procedure was only about 10%.

The $^{10}\text{Be}/\text{Be}$ ratios were also measured at the PSI-ETH AMS facility. Based on published cross sections (Bodemann et al., 1993), the production of ^{10}Be in the aluminum windows can also be neglected ($\leq 1\%$ relative to the production in nitrogen).

The adsorption of the produced nuclides on the aluminum foil was found to be very efficient. For ^7Be , the activity on the filter was less than 1% of the total measured activity. For ^{36}Cl , the measured $^{36}\text{Cl}/\text{Cl}$ ratio on the filter was identical to the chemistry blank value (about $5 \cdot 10^{-14}$). This is reasonable, since the aluminum oxide surface adsorbs cations as well as anions.

For irradiations of pure argon or nitrogen, the same procedure was used. After the hydroxide precipitation, both fractions were separated, and the hydroxides were discarded for pure argon samples whereas for pure nitrogen samples the liquid phase was discarded. Figure 3.7 summarizes the chemical procedure applied to the samples.

During some PIF irradiations, nickel foils were introduced into the beam line behind and in front of the target. These foils were folded to a square of about 4 cm length and their activities were measured on a germanium detector at a distance of 15 cm.

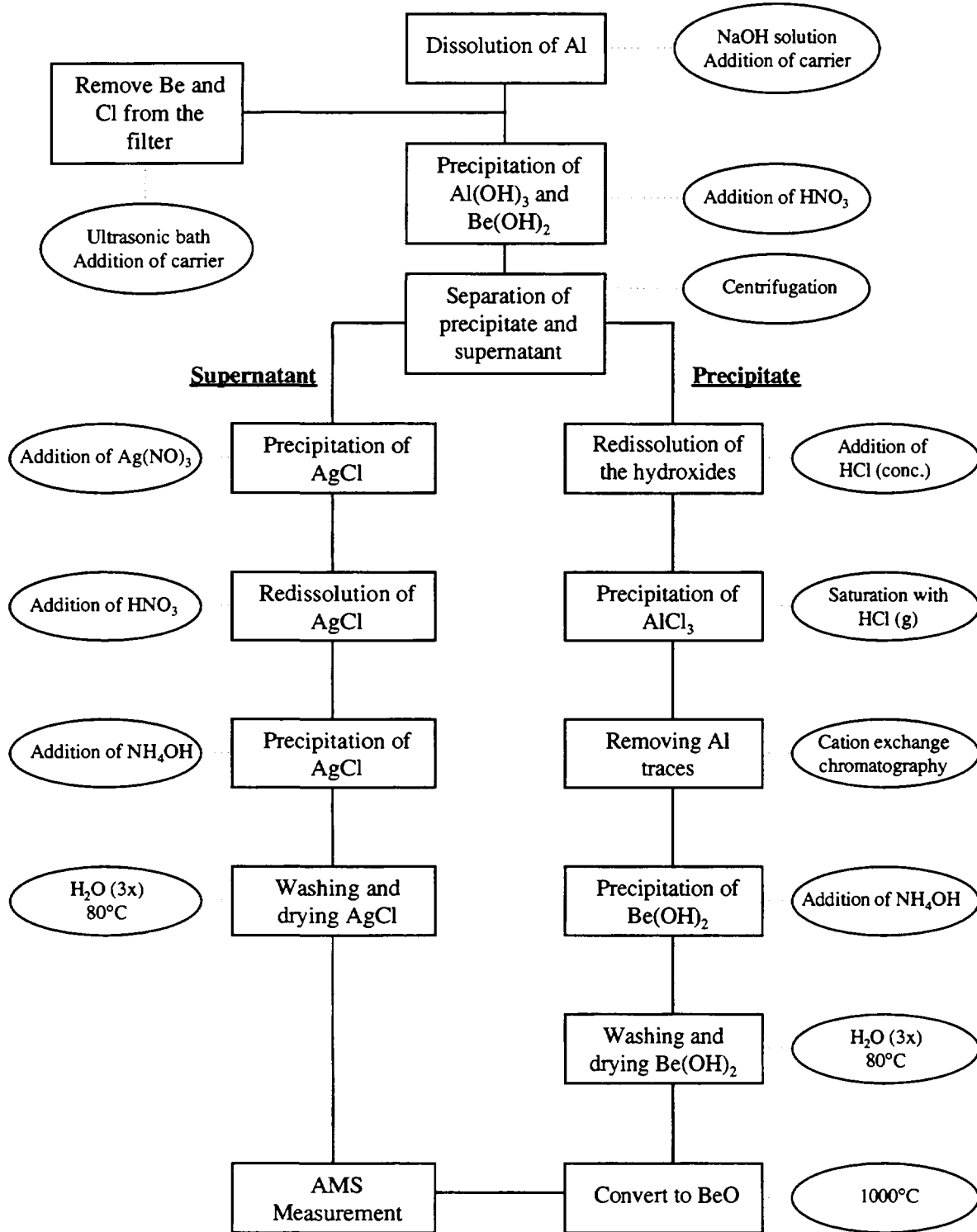


Figure 3.7: Summary of the chemistry steps applied to the samples.

3.5 Results and discussion

3.5.1 Proton induced cross sections on nickel targets

Nickel foils were additionally introduced into the beam line in order to test the accuracy of the proton fluxes measurements through ionization chambers. If cross sections of proton induced reactions on nickel were known with accuracy, they could also be suitable as proton flux monitors for low fluxes, when the monitoring reaction $^{27}\text{Al}(p,3p3n)^{22}\text{Na}$ could not be used.

These foils were bombarded during six different irradiations, at the energies 46.7 MeV, 60.4 MeV, 77.2 MeV and 141.2 MeV. The energy loss between the two windows for the bombardment at 46.7 MeV was large enough to deduce different cross sections in each window corresponding to energies of 44 MeV and 49.3 MeV. Three irradiations were carried out at 77.2 MeV. The activities of the five following nuclides were measured: ^{57}Ni ($T_{1/2} = 36.0$ h), ^{56}Co ($T_{1/2} = 78.8$ d), ^{55}Co ($T_{1/2} = 17.5$ h), ^{52}Fe ($T_{1/2} = 8.27$ h) and ^{52}Mn ($T_{1/2} = 5.59$ d). However, cross sections for the reaction $\text{Ni}(p,X)^{52}\text{Mn}$ were not deduced, since ^{52}Mn is also produced via β -decay of ^{52}Fe , which was also produced in the nickel foils.

The cross sections were calculated according to eq. 3.6:

$$\sigma_i = \frac{A_i \cdot t_{irr}}{N_p \cdot N_T \cdot x_T \cdot (1 - e^{-\lambda_i \cdot t_{irr}})} \quad (3.13)$$

Where: Φ_p , the proton flux, is substituted by N_p/t_{irr}

A_i is the weighted mean of the activities measured with the different γ -lines of each produced nuclides behind and in front of the target

The cross sections for the reactions $\text{Ni}(p,X)^{57}\text{Ni}$, $\text{Ni}(p,X)^{56}\text{Co}$, $\text{Ni}(p,X)^{55}\text{Co}$ and $\text{Ni}(p,X)^{52}\text{Fe}$ are listed in table 3.5 and compared with literature data in figures 3.8 to 3.11.

Table 3.5: Proton induced cross sections on nickel targets.

Energy [MeV]	Reaction cross sections [mb]			
	$\text{Ni}(p,X)^{57}\text{Ni}$	$\text{Ni}(p,X)^{56}\text{Co}$	$\text{Ni}(p,X)^{55}\text{Co}$	$\text{Ni}(p,X)^{52}\text{Fe}$
44.0 ± 7.8	74.01 ± 6.22	118.17 ± 16.80	16.40 ± 1.38	0.37 ± 0.11
49.3 ± 7.8	76.69 ± 6.15	152.29 ± 18.85	22.06 ± 1.57	0.65 ± 0.11
60.4 ± 5.9	65.92 ± 3.90	121.67 ± 11.36	27.26 ± 1.41	1.14 ± 0.14
77.2 ± 5.1	60.91 ± 2.07	122.26 ± 7.29	26.87 ± 0.79	1.45 ± 0.09
141.2 ± 3.4	43.85 ± 2.73	73.54 ± 7.77	19.77 ± 1.06	2.00 ± 0.25

The measured cross sections of the reaction $\text{Ni}(p,X)^{57}\text{Ni}$ shown in figure 3.8 do not agree with the values measured by Aleksandrov et al. (1987) in the same energy range. However, they represent a good fit between the values measured by Michel et al. (1978) and Schieckel et al. (1996), and the cross sections measured at 44.0 and 49.3 MeV are in excellent agreement with the value of Michel et al. (1978) at 44.7 MeV.

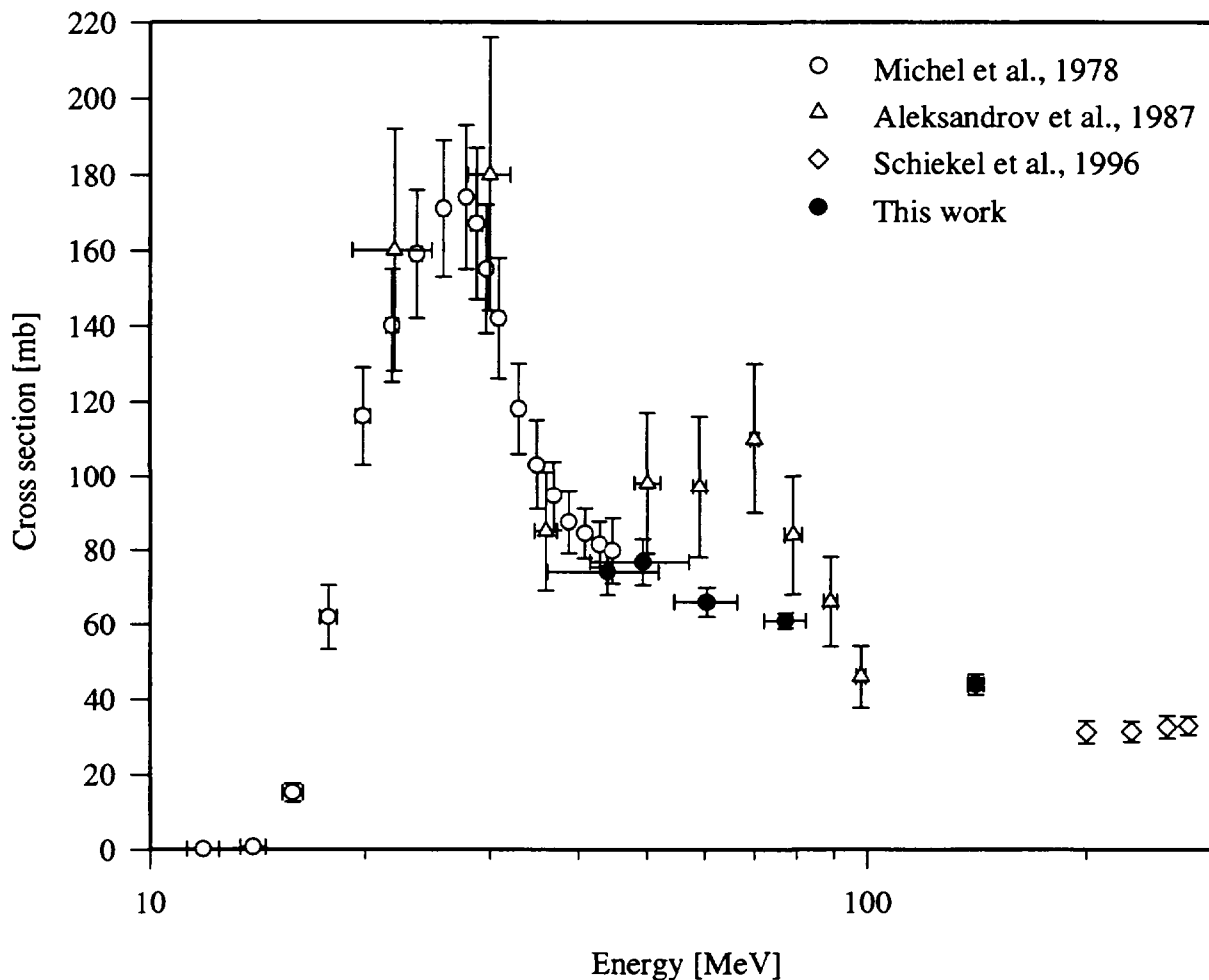


Figure 3.8: Cross sections of the reaction $\text{Ni}(p,X)^{57}\text{Ni}$.

The measured cross sections of the reaction $\text{Ni}(p,X)^{56}\text{Co}$ (see figure 3.9) are also lower than those of Aleksandrov et al. (1987), but in this case, except for the value measured at 44.0 MeV, they still agree within experimental errors. Again, our values fit well between those of Michel et al. (1978) and Schieckel et al. (1996).

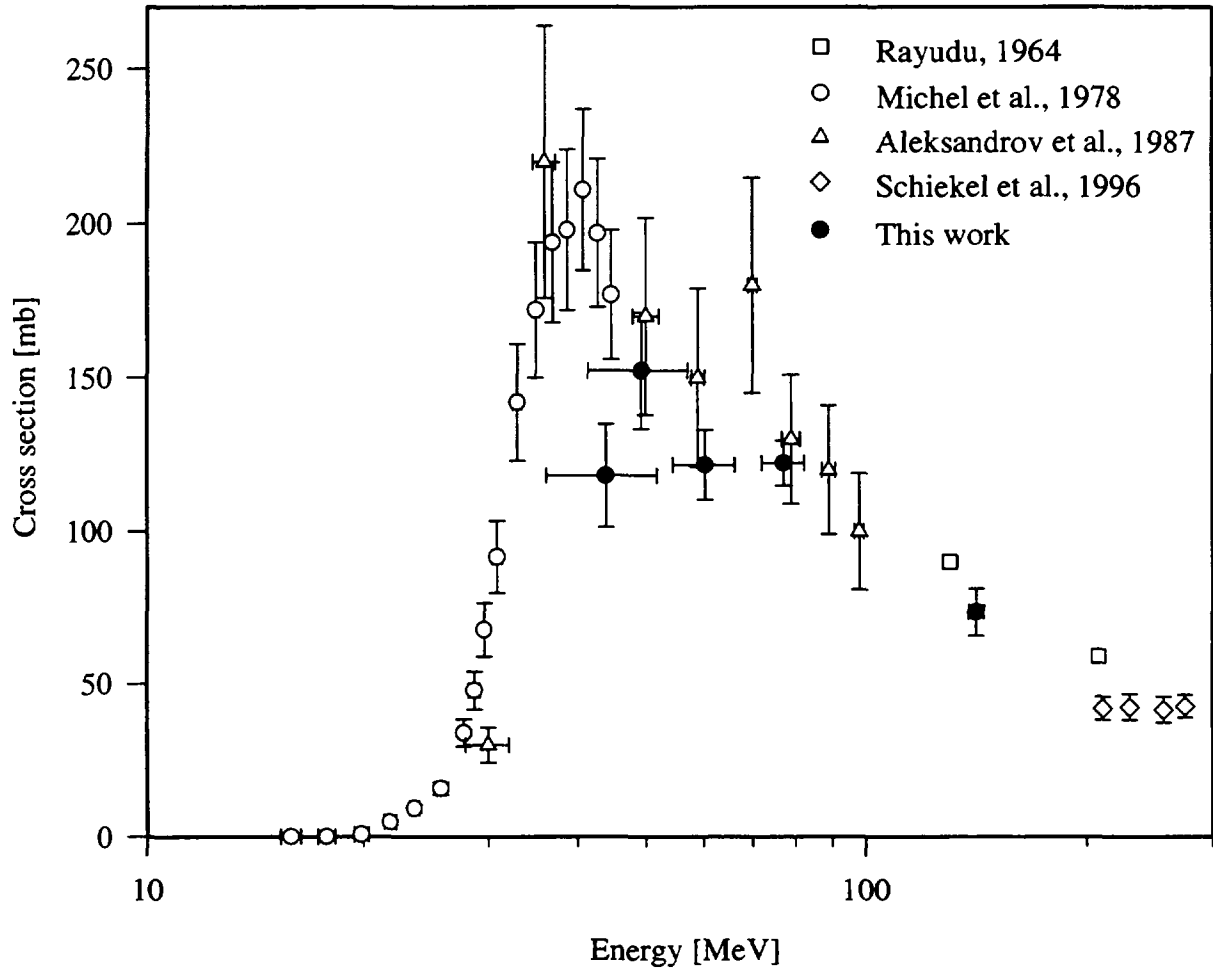


Figure 3.9: Cross sections of the reaction $\text{Ni}(p,X)^{56}\text{Co}$.

For the reaction $\text{Ni}(p,X)^{55}\text{Co}$ (see figure 3.10), a very good agreement is found between the cross sections measured at 44.0 MeV and 49.3 MeV and those measured by Michel et al. (1978) at 42.8 MeV and 44.7 MeV. The measured excitation function shows two maxima. For the second maximum, at an energy of about 65 MeV, our measured cross section of about 27 mb disagrees significantly from the value of 70 mb measured by Tanaka et al. (1972). However, the cross sections for the first maximum from Tanaka et al. (1972) were also higher compared to the more recent values obtained by Tarkanyi et al. (1991).

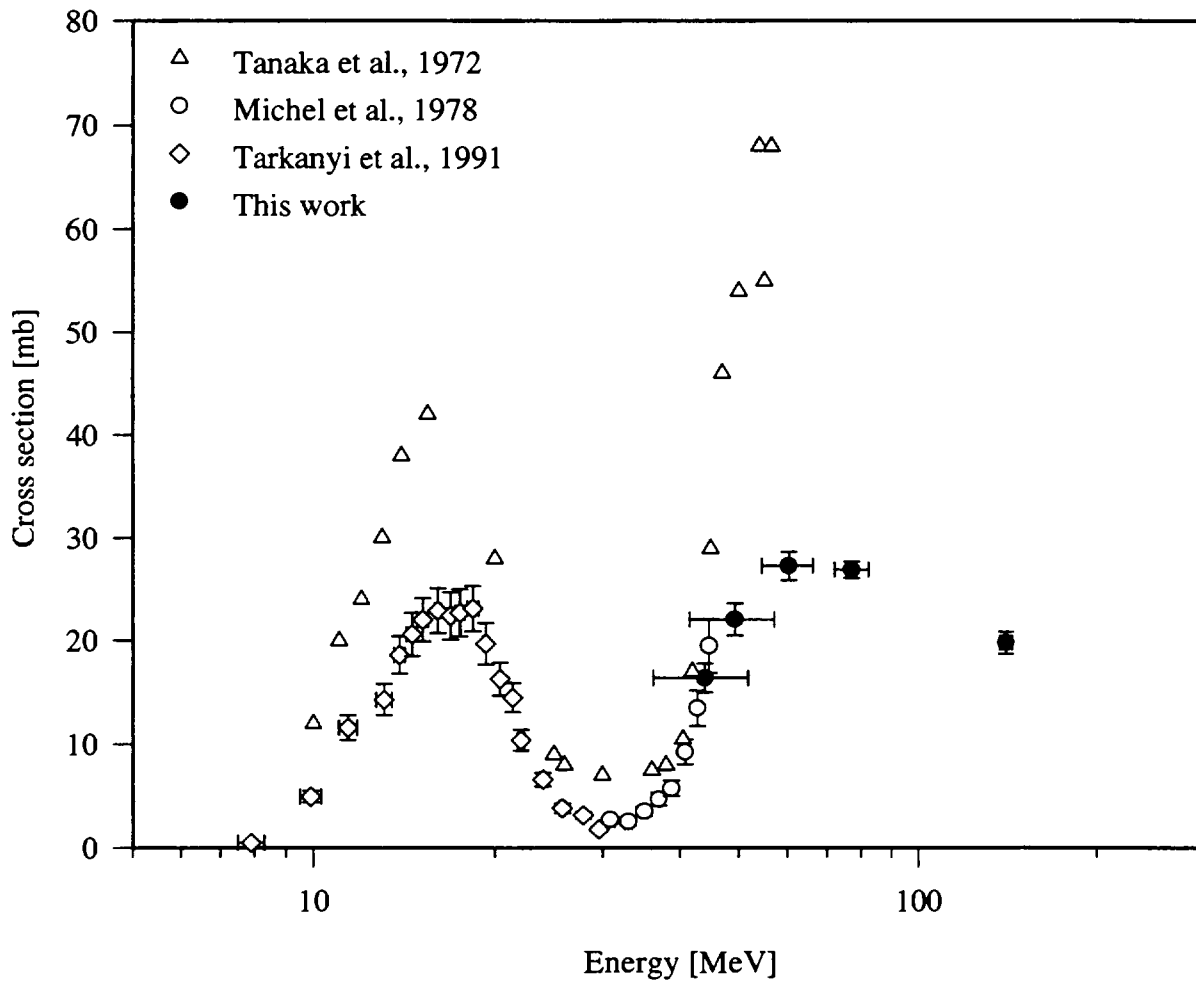


Figure 3.10: Cross sections of the reaction $\text{Ni}(p,X)^{55}\text{Co}$.

In figure 3.11, the measured cross sections of the reaction $\text{Ni}(p,X)^{52}\text{Fe}$ are compared to the excitation function measured by Steyn et al. (1990). The cross sections at 46.7 MeV, 60.4 MeV and 141.2 MeV agree within the experimental error with this excitation function. However, for unknown reasons, the peak measured by Steyn et al. (1990), with a maximum at about 60 MeV, is not observed in our work.

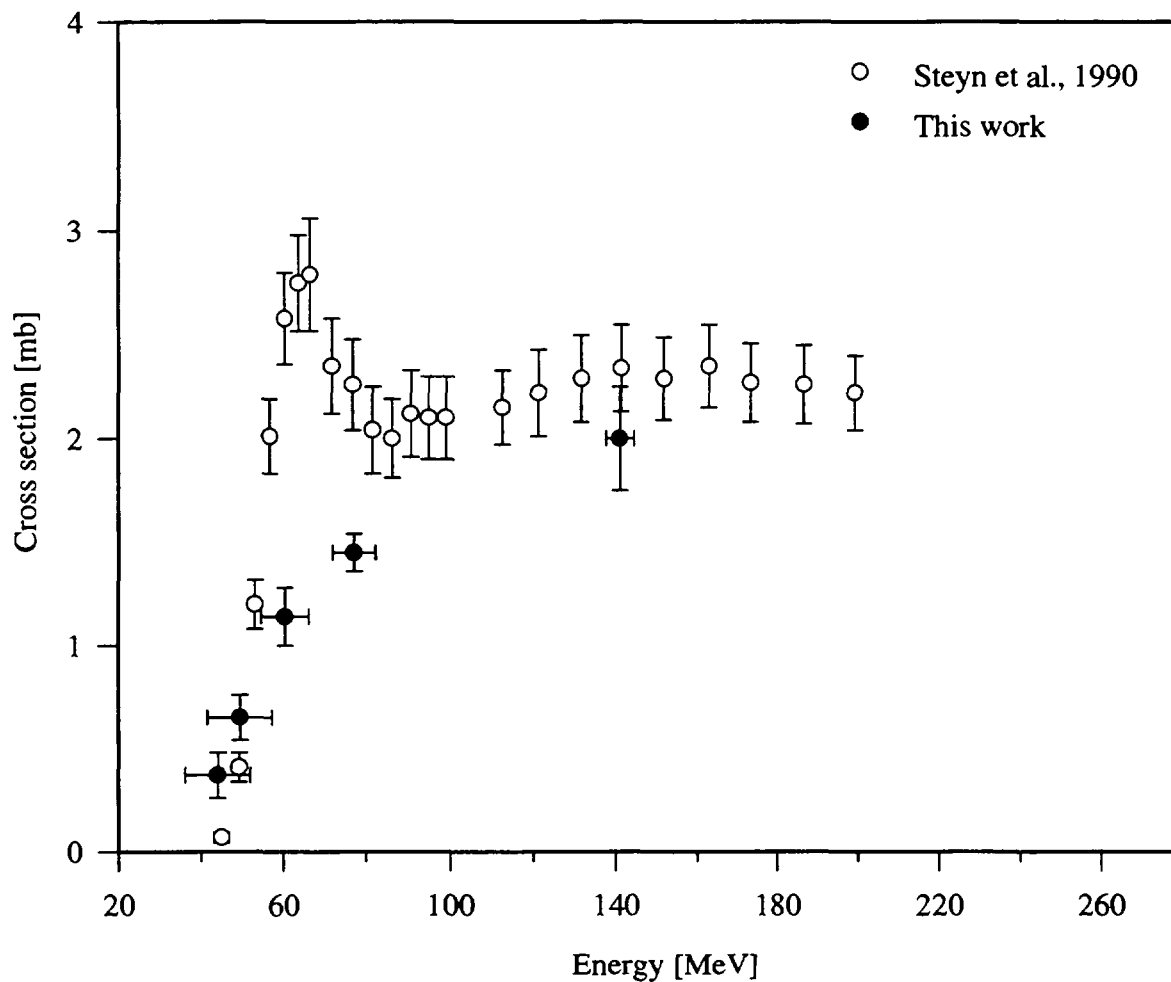


Figure 3.11: Cross sections of the reaction $\text{Ni}(p,X)^{52}\text{Fe}$.

As a general conclusion, from the intercomparison of our data with literature values, one can consider the proton flux monitoring during the Proton Irradiation Facility irradiations as satisfactory. Indeed, the majority of the measured data agree well with existing literature values. Therefore, more cross section measurements are needed to use nuclear reactions on nickel as a proton flux monitor. There are still too large discrepancies in the existing data set.

3.5.2 Proton induced cross sections in gas targets

The cross sections for the reaction $N(p,X)^7\text{Be}$ were calculated with eq. 3.14. Since ^{10}Be and ^{36}Cl have very long half-lives, for the reactions $N(p,X)^{10}\text{Be}$ and $^{40}\text{Ar}(p,X)^{36}\text{Cl}$, the cross sections were calculated using eq. 3.8:

$$\sigma_i = \frac{N_i}{N_p \cdot N_T \cdot x_T} \cdot 10^{-27} \quad (3.14)$$

Where: σ_i : Cross section [mb]

N_i : Number of produced atoms (measured with AMS)

N_p : Number of protons which passed through the target

N_T : Atomic density of the gas in the target [cm^{-3}]

x_T : Length of the target [cm]

Most of the gas target irradiations were carried out twice. In general, both measured cross sections agreed within $\pm 4\%$ (of the mean value) for ^7Be , $\pm 13\%$ for ^{10}Be , and $\pm 3\%$ for ^{36}Cl , respectively, showing that the measurements were very reproducible. The relatively high discrepancy for ^{10}Be is due to the small $^{10}\text{Be}/\text{Be}$ ratios of about 10^{-13} . A large amount of carrier had been added because of the poor yield of the ^{10}Be extraction, which led to high errors. Nevertheless, the duplicate measurements always agreed within experimental error.

Table 3.6: Reaction cross sections measured in gas targets.

Energy [MeV]	Reaction cross sections [mb]		
	$N(p,X)^7\text{Be}$	$N(p,X)^{10}\text{Be}$	$^{40}\text{Ar}(p,X)^{36}\text{Cl}$
12.91 ± 0.82	0.21 ± 0.08		0.51 ± 0.24
25.39 ± 0.60	24.34 ± 2.94		105.41 ± 8.94
32.76 ± 0.53	7.29 ± 0.84		42.76 ± 3.27
40.36 ± 0.48	6.99 ± 0.73	0.04 ± 0.01	18.72 ± 1.45
46.70 ± 7.80			32.90 ± 2.44
59.62 ± 0.41	8.73 ± 0.88	0.13 ± 0.03	40.81 ± 2.71
60.40 ± 5.90			40.15 ± 2.66
77.20 ± 5.10			47.76 ± 3.10
94.70 ± 4.40			53.45 ± 4.89
118.20 ± 3.80			45.05 ± 4.23
141.20 ± 3.40			39.87 ± 4.04
188.50 ± 3.00			34.16 ± 2.53
292.20 ± 1.20			25.01 ± 2.90
302.33 ± 1.10	10.01 ± 1.24	1.04 ± 0.20	
587.87 ± 0.36			21.58 ± 4.43
587.99 ± 0.27	9.38 ± 1.36		

The results are presented in Table 3.6 and for ${}^7\text{Be}$ and ${}^{10}\text{Be}$ in figure 3.12 and 3.13 compared to existing literature data from solid targets. The measured cross sections are also compared with two models: a semi-empirical spallation model (Silberberg and Tsao, 1973) and a hybrid model of preequilibrium reactions in form of the code ALICE 900 (Michel and Blann, 1993).

Figure 3.12 shows that the measured cross sections of the reaction $N(p,X){}^7\text{Be}$ are in good agreement with cross sections deduced from solid targets. This shows that the gas target technique is very suitable for such cross sections measurements. However, the agreement between measured data and both models is poor. Such a disagreement was also observed between measured cross sections and the preequilibrium decay model by Bodemann et al. (1993) for light targets. Better agreements between experimental and theoretical results were obtained for medium-heavy elements up to about 200 MeV (Michel et al., 1985; Fink et al., 1990). At higher energies, the interaction between protons and the targets can no more be explained by preequilibrium decay, since direct interactions occur. The direct interaction model of Silberberg and Tsao (1973), which is valid for energies higher than 100 MeV, does not give satisfactory results, however.

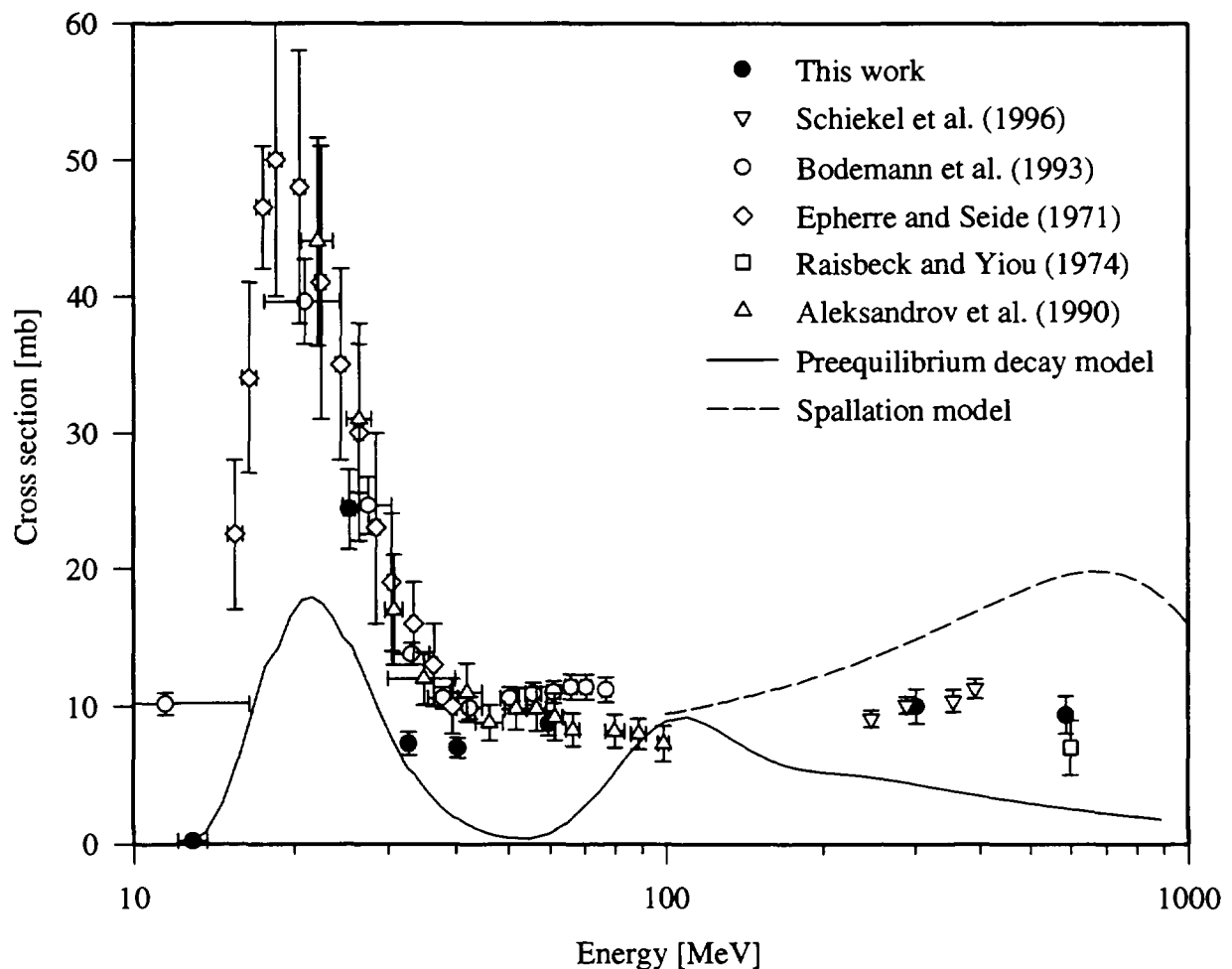


Figure 3.12: Cross sections of the reaction $N(p,X){}^7\text{Be}$.

The same comments are valid for the reaction $N(p,X)^{10}\text{Be}$ (see figure 3.13): the measured cross sections agree well with cross sections measured in solid targets, but not with either model.

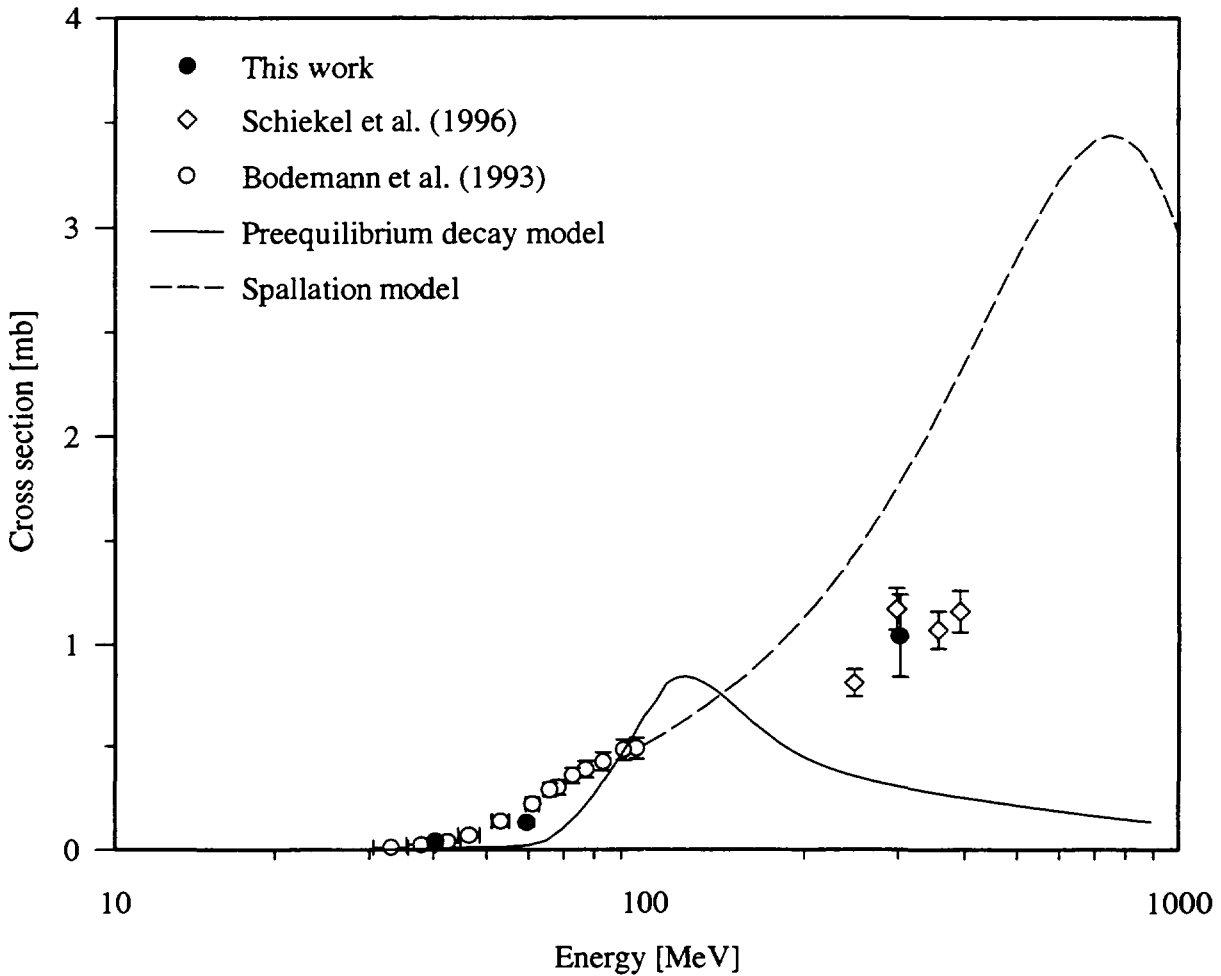


Figure 3.13: Cross sections of the reaction $N(p,X)^{10}\text{Be}$.

The measured excitation function of the reaction $^{40}\text{Ar}(p,X)^{36}\text{Cl}$ (see figure 3.14) shows two maxima. The first one, at an energy of about 20 MeV, corresponds to a $(p,\alpha n)$ reaction with a maximum cross section of 105 mb. The second one, at an energy of about 100 MeV corresponds to an uncorrelated emission of two protons and three neutrons and has a maximum cross section of 53 mb. These two maxima are also predicted by the preequilibrium decay model, but with higher cross sections. The first peak could lead to a non negligible production of ^{36}Cl through solar cosmic rays, since SCR's are low in energy but very intensive.

The results of the two irradiations at 59.6 MeV and 60.4 MeV carried out at the Philips Cyclotron and the Proton Irradiation Facility, respectively, agree well. This again shows, that the proton flux measurements carried out with ionization chambers during the PIF irradiations yielded reliable values.

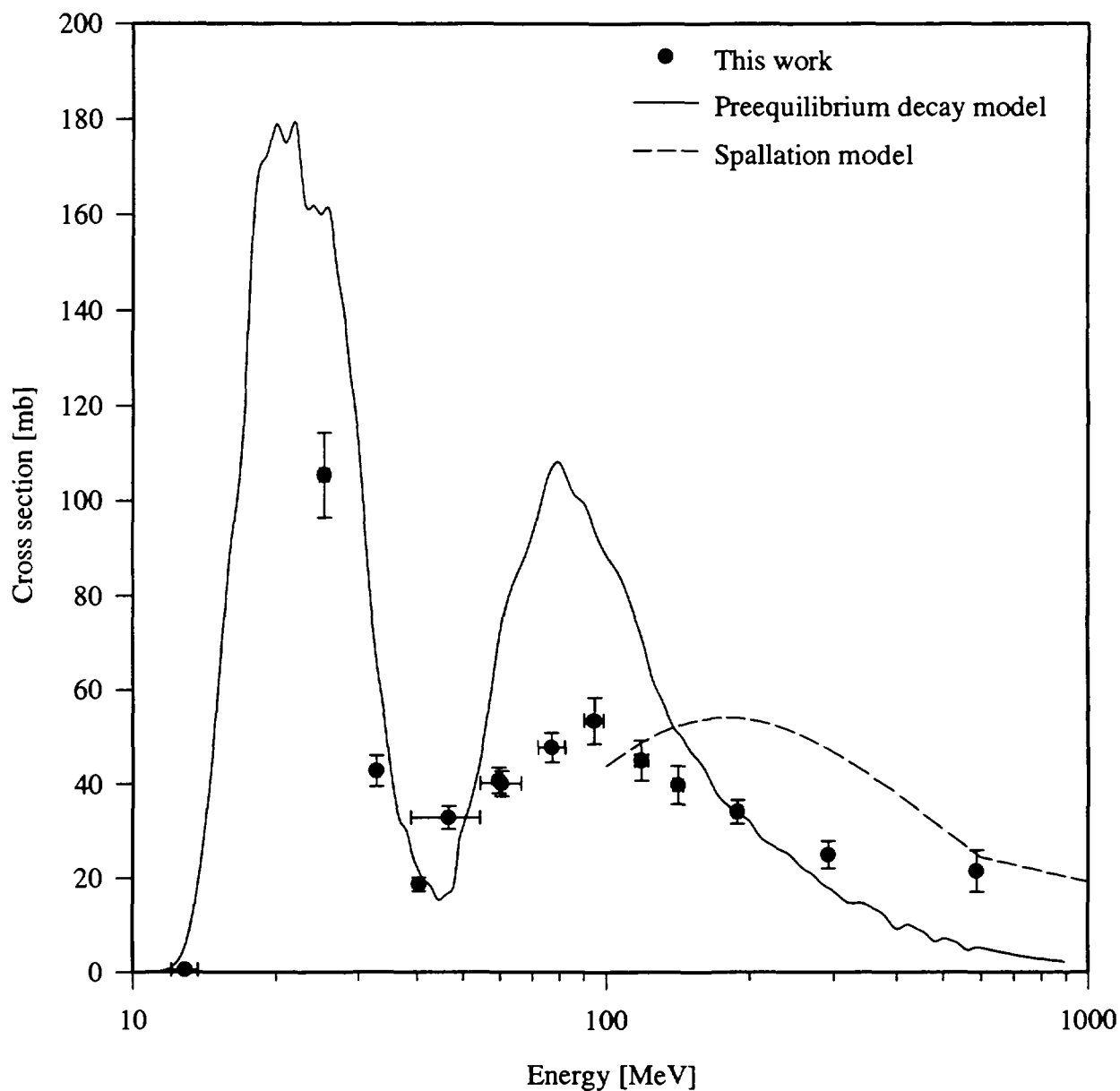


Figure 3.14: Cross sections of the reaction $^{40}\text{Ar}(p,X)^{36}\text{Cl}$.

The larger relative error of the cross section at 590 MeV compared to those at lower energies is due to a problem during the chemistry procedure. During the last beam time at PIF, four targets were irradiated (samples WQCL 14 to WQCL 17): two at an energy of 590 MeV, as well as one at about 300 MeV and one at about 200 MeV to be compared with previous results. The measured cross sections at these two lower energies turned out to be higher than the results of the first measurements by a factor of 1.4. This was assigned to a problem during addition of the chlorine carrier. The measured cross sections at 590 MeV were therefore divided by this factor of 1.4.

The Monte-Carlo simulation used to calculate the proton fluxes was also used to calculate the energy spectrum of the neutrons produced in the 50 cm air between the beam pipe and the target

front. The results showed that production of the nuclides of interest by neutrons was negligible, since most of them had an energy smaller than the reaction thresholds. In the worst case, less than 3% of the production could be due to neutrons, which is within experimental error.

3.6 Conclusions

A new cross section data set for proton-induced reactions on nickel has been measured. It covers the energy range between 40 and 150 MeV, where only a few literature data already exist. The complete data set could lead to a future use of nickel foils to monitor low proton fluxes which cannot be monitored with the reaction $^{27}\text{Al}(p,3p3n)^{22}\text{Na}$.

By comparison with literature data obtained by solid target irradiations, the measured cross sections of the reactions $\text{N}(p,X)^7\text{Be}$ and $\text{N}(p,X)^{10}\text{Be}$ have shown that the gas target method is very suitable. It has the advantage that pure atmospheric gases can be irradiated without interfering reactions such as in case of solid targets.

For the first time, cross sections of the reaction $^{40}\text{Ar}(p,X)^{36}\text{Cl}$ have been measured. Some preliminary cross sections of the bombardments described in this work have already been published previously (Huggle et al., 1996). For these values, the $^{36}\text{Cl}/\text{Cl}_{\text{tot}}$ ratios were measured with the AMS facility at Munich, whereas the $^{36}\text{Cl}/\text{Cl}_{\text{tot}}$ ratios of the samples from this work were measured with the AMS facility at Zurich. Our data yield a very high cross section of 105 mb at an energy of about 20 MeV, which could lead to an important atmospheric production of ^{36}Cl by solar cosmic rays. As a consequence, the variability of the $^{10}\text{Be}/^{36}\text{Cl}$ ratios measured in Greenland ice cores (Suter et al., 1987; Elmore et al., 1987), which was assigned to different atmospheric transport processes of both nuclides, could also be due to partially different production channels. Indeed, ^{10}Be has no low energy peak in its excitation function. Hence, it cannot be produced by solar cosmic rays. The $^{10}\text{Be}/^{36}\text{Cl}$ ratio could therefore have a new application, namely a marker to reconstruct the history of important solar flares, since such events should lead to a decrease of the $^{10}\text{Be}/^{36}\text{Cl}$ ratio by increasing the production of ^{36}Cl .

4. Atmospheric production rate of ^{36}Cl

The importance of the ^{36}Cl deposition rate has been discussed in chapter 3. In the following, the measured cross sections of the reaction $^{40}\text{Ar}(p,X)^{36}\text{Cl}$ and the neutron and proton energy spectra of Flückiger (1976) are used to calculate the production rate of ^{36}Cl in the atmosphere. Due to the lack of experimental atmospheric proton and neutron energy spectra induced by primary solar protons, the following chapters will discuss only the ^{36}Cl atmospheric production through galactic cosmic rays. The deposition model of Lal and Peters (1967) and the production rates calculated in this work are then used to predict a latitudinal dependence of the ^{36}Cl deposition rate.

4.1 Calculation of the atmospheric production rate of ^{36}Cl

The atmospheric production rate P_j of a long-lived cosmogenic radionuclide j at a latitude corresponding to a vertical cutoff rigidity R_{cv} is given by:

$$P_j(R_{cv}) = \sum_t \sum_i \int_E \int_h J_i(E, R_{cv}, h) \cdot \sigma_{i,j,t}(E) \cdot N_t(h) \cdot dE \cdot dh \quad (4.1)$$

Where: $J_i(E, R_{cv}, h)$: Omnipotential¹ energy spectrum of an incident particle i at a cutoff rigidity R_{cv} and an atmospheric depth h [$\text{cm}^{-2} \cdot \text{s}^{-1} \cdot \text{MeV}^{-1}$]

$\sigma_{i,j,t}(E)$: Cross section of the reaction $t(i, X)j$ at an energy E , t being the target [cm^2]

$N_t(h)$: Concentration of the target at an atmospheric depth h , in [$\text{g} \cdot \text{cm}^{-2}$], [g^{-1}]

The proton and neutron high energy spectra in the atmosphere were obtained from a Monte-Carlo simulation (Flückiger, 1976). This model simulates the particle cascade in the atmosphere for a galactic primary proton energy spectrum at a mean solar activity. The cascade is influenced by the following parameters:

¹ An omnipotential particle flux is a flux which crosses a sphere with unity surface.

- energy dependent neutron mean free path and π -meson mean free path of 75 gcm^{-2} .
- ionization losses
- elastic and inelastic neutron diffusion
- π -meson-neutron diffusion
- π -meson absorption
- atmospheric composition

The Monte-Carlo simulation calculates the differential energy spectra, $I_i(\theta, E, h, R_{cv})$, of neutrons and protons for different latitudes and altitudes in the energy range 50 MeV-100 GeV. Eq. 4.2 allows to calculate the omnipotential energy spectra:

$$J_i(E, h, R_{cv}) = 2\pi \cdot \int_0^{\pi/2} I_i(\theta, E, h, R_{cv}) \cdot \sin\theta \cdot d\theta \quad (4.2)$$

Where: $I_i(\theta, E, h, R_{cv})$: differential energy spectrum at an atmospheric depth h and a latitude corresponding to a vertical cutoff rigidity R_{cv} [$\text{cm}^{-2}\text{s}^{-1}\text{sr}^{-1}\text{MeV}^{-1}$]
 θ : Zenith angle of the particles

Since the calculated proton energy spectra do not range below 50 MeV, where high reaction cross sections were measured (see Chapter 3), these proton spectra were extended to 10 MeV by comparison with literature data. Measured proton energy spectra (Barber et al., 1980; Brooke and Wolfendale, 1964; Kocharian et al., 1959; Filthuth, 1955; Mylroi and Wilson, 1951) show that the maxima of the spectra lie between 100 and 300 MeV, for all altitudes and latitudes. The spectra of Flückiger (1976) were therefore extended to lower energies by fitting them on a logarithmic scale with a second order polynomial normalized to the maximum values at 200 MeV (see figures 4.1 and 4.2). These fits agree with measured data only in the energy range above about 100 MeV. To obtain a better agreement in the 10-100 MeV energy range, a linear regression on a logarithmic scale was carried out between 10 and 200 MeV. Examples of resulting predicted proton spectra are shown in figures 4.1 and 4.2. To be compared with literature data, the vertical intensities are plotted as a function of the energy. The same fitting procedures were applied to the omnipotential spectra.

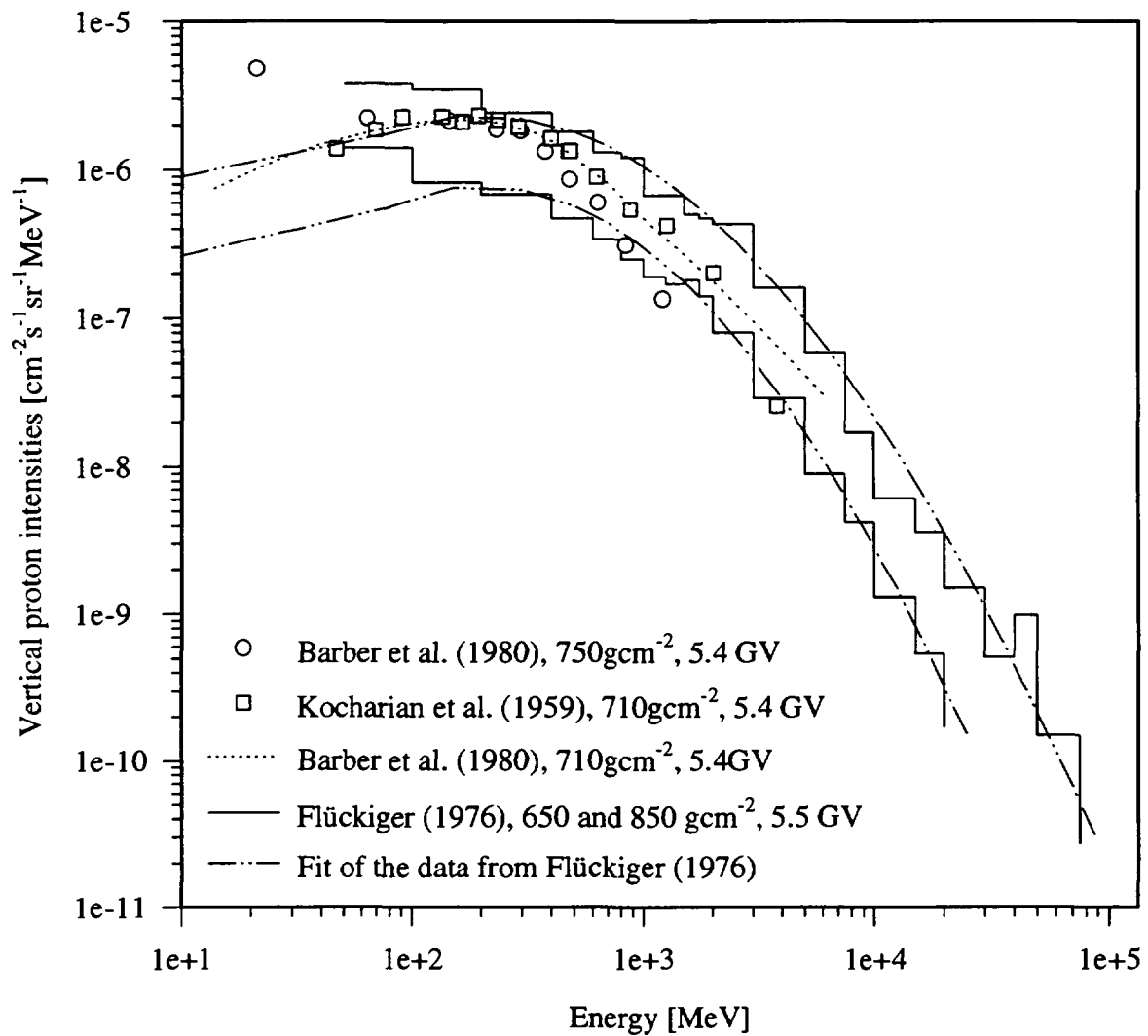


Figure 4.1: Proton spectra obtained from a Monte-Carlo simulation (Flückiger, 1976, solid lines) compared to measured (symbols) and theoretical (dashed-dotted lines) spectra for an atmospheric depth between 650 (top) and 850gcm^{-2} (bottom) and a vertical cutoff rigidity of 5.4 to 5.5GV .

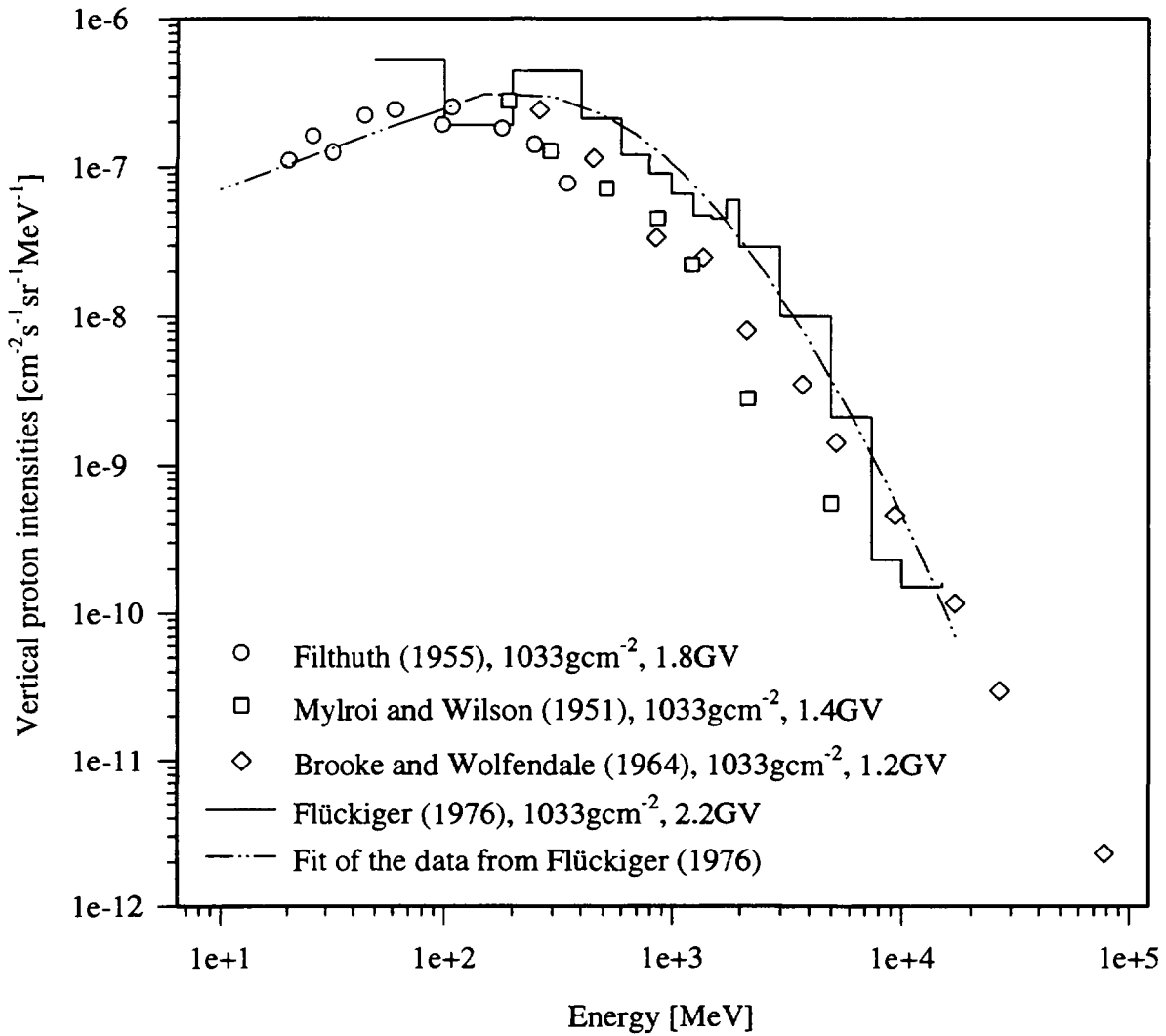


Figure 4.2: Proton spectra obtained from a Monte-Carlo simulation (Flückiger, 1976, solid line) compared to measured (symbols) and theoretical (dashed-dotted line) spectra for an atmospheric depth of 1033gcm^{-2} and a vertical cutoff rigidity lying between 1.2 and 2.2 GV.

No extension in the low energy range for the neutron energy spectra is needed, since the reaction $^{40}\text{Ar}(n,X)^{36}\text{Cl}$ has a threshold energy of 37 MeV. The same intensities were adopted between 37 and 50 MeV as for 50 MeV. However, the Monte-Carlo simulation yielded too low values in the 50-5000 MeV energy range (see figure 4.3). The calculated values were therefore adjusted to the experimental data (Armstrong et al., 1973; Merker, 1973; Preszler et al., 1974). For a given latitude, independent of the altitude, the differences between the intensities calculated by the Monte-Carlo simulation and literature data were plotted as a function of the energy. The obtained resulting curve was used to correct the neutron energy spectrum. An example of such a corrected spectrum is shown in figure 4.3.

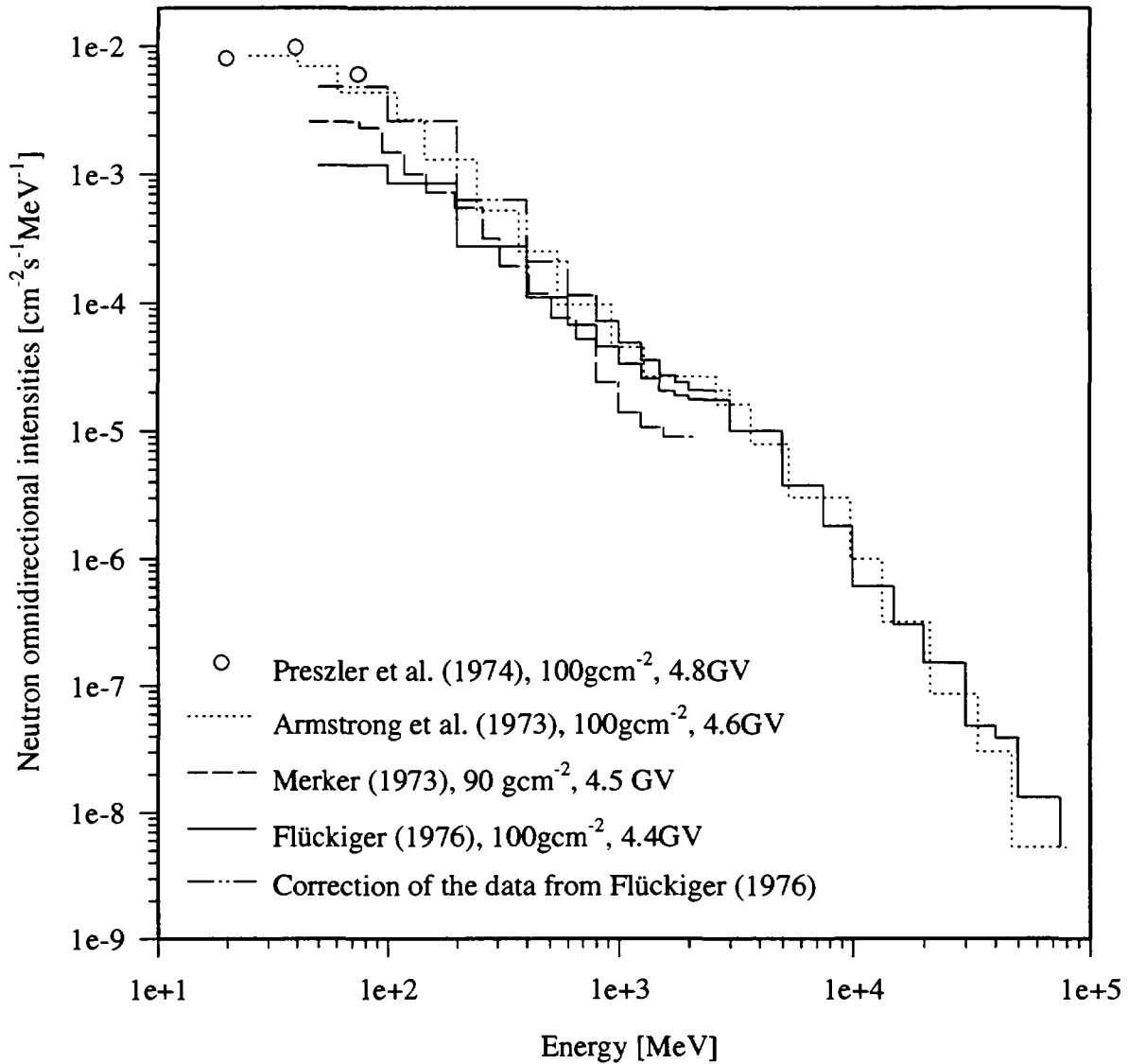


Figure 4.3: Neutron spectra obtained from a Monte-Carlo simulation (Flückiger, 1976, solid line) compared with measured (symbols) and theoretical (dashed-dotted lines) spectra for an atmospheric depth of about 100gcm^{-2} and a vertical cutoff rigidity lying between 4.4 and 4.8 GV.

Three reactions can produce ^{36}Cl in the atmosphere, i.e. $^{40}\text{Ar}(p,X)^{36}\text{Cl}$ and $^{40}\text{Ar}(n,X)^{36}\text{Cl}$ at high energies, and $^{36}\text{Ar}(n,p)^{36}\text{Cl}$ at low energies. The cross sections for the reaction $^{40}\text{Ar}(p,X)^{36}\text{Cl}$ are taken from Chapter 3. For the reaction $^{40}\text{Ar}(n,X)^{36}\text{Cl}$, the cross sections were calculated by Masarik (1996) using the LAHET code (Prael and Liechtenstein, 1989). The simulation for high energy particles is based on the intranuclear cascade model of Bertini (1969). An optional multistage preequilibrium exciton model (Prael and Bozoian, 1988) has been implemented to the LAHET Code as an intermediate stage between the intranuclear cascade and the evaporation phase of a nuclear interaction. This is of great importance in the energy range of interest, i.e. between 50-500 MeV.

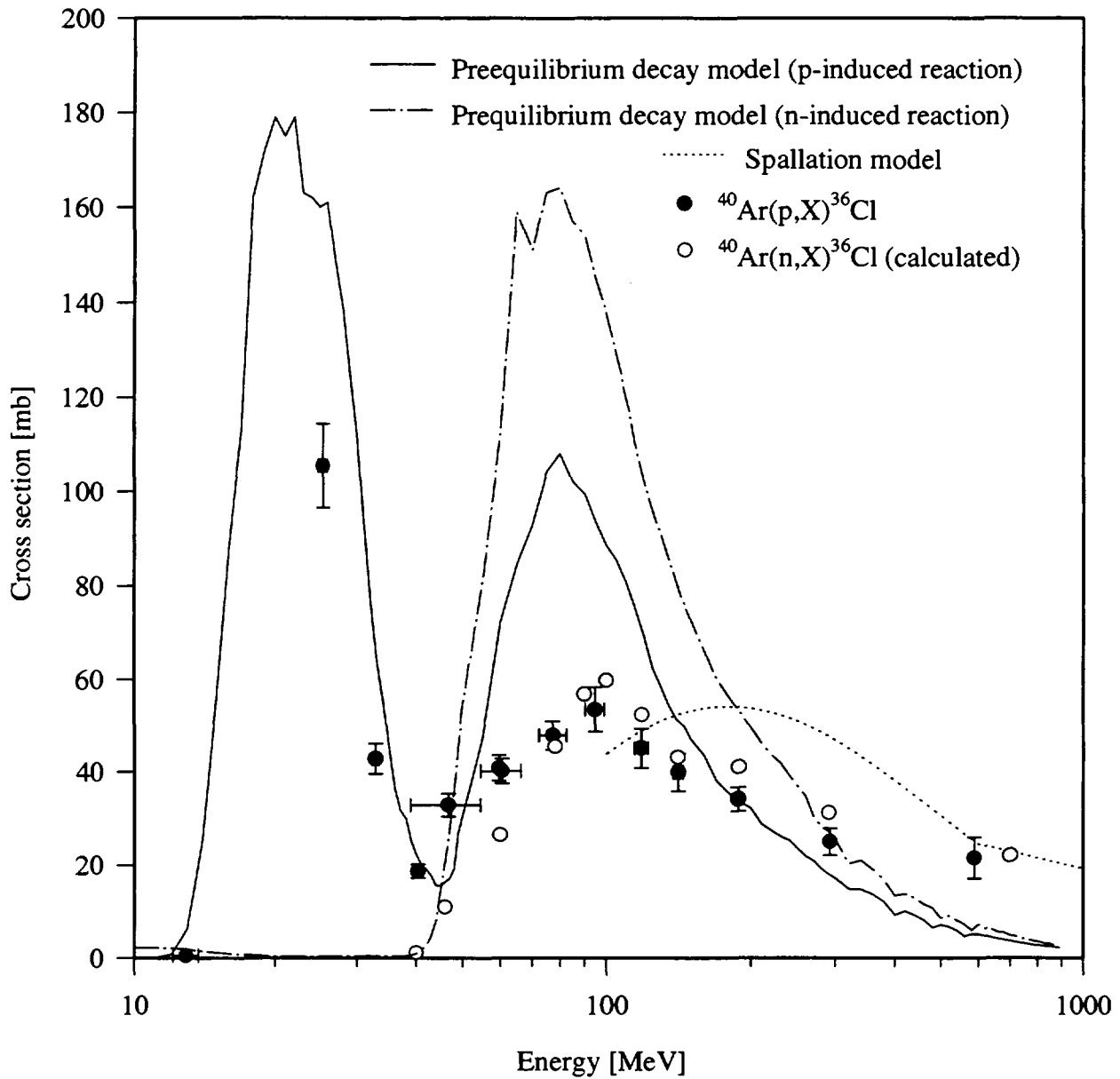


Figure 4.4: Cross sections of the reaction $^{40}\text{Ar}(n,p)^{36}\text{Cl}$ compared to the preequilibrium decay model and to the cross sections deduced from the proton-induced reaction.

For the reaction $^{36}\text{Ar}(n,p)^{36}\text{Cl}$, the cross sections were taken from Davis et al. (1964), Gardner and Rosenblum (1967) and Jiang et al. (1990). Since this reaction is essentially induced by slow neutrons with energies lower than 10 MeV, and since the Monte-Carlo simulation gives no neutron flux for energies lower than 50 MeV, the neutron spectra of Armstrong et al. (1973) were used, which range between 10^{-7} and 10^3 MeV.

To facilitate integration, eq. 4.1 was decomposed and integrated in two steps. First, the altitudinal dependence of the production rate was calculated:

$$P_j(R_{cv}, h) = \sum_i \sum_t \int E J_i(E, R_{cv}, h) \sigma_{i,j,t}(E) \cdot N_t(h) \cdot dE \quad (4.3)$$

The results of this integration consist in local production rates, i.e. production rates at one point of the atmosphere defined by its latitude and altitude. The neutron and proton energy spectra calculations using the Monte-Carlo simulation were performed for six different cutoff rigidities (2.2, 3.2, 4.4, 5.5, 7.0 and 14.9 GV) and seven different altitudes (40, 100, 160, 350, 650, 850 and 1033 gcm^{-2}) yielding 42 local production rates in the atmosphere.

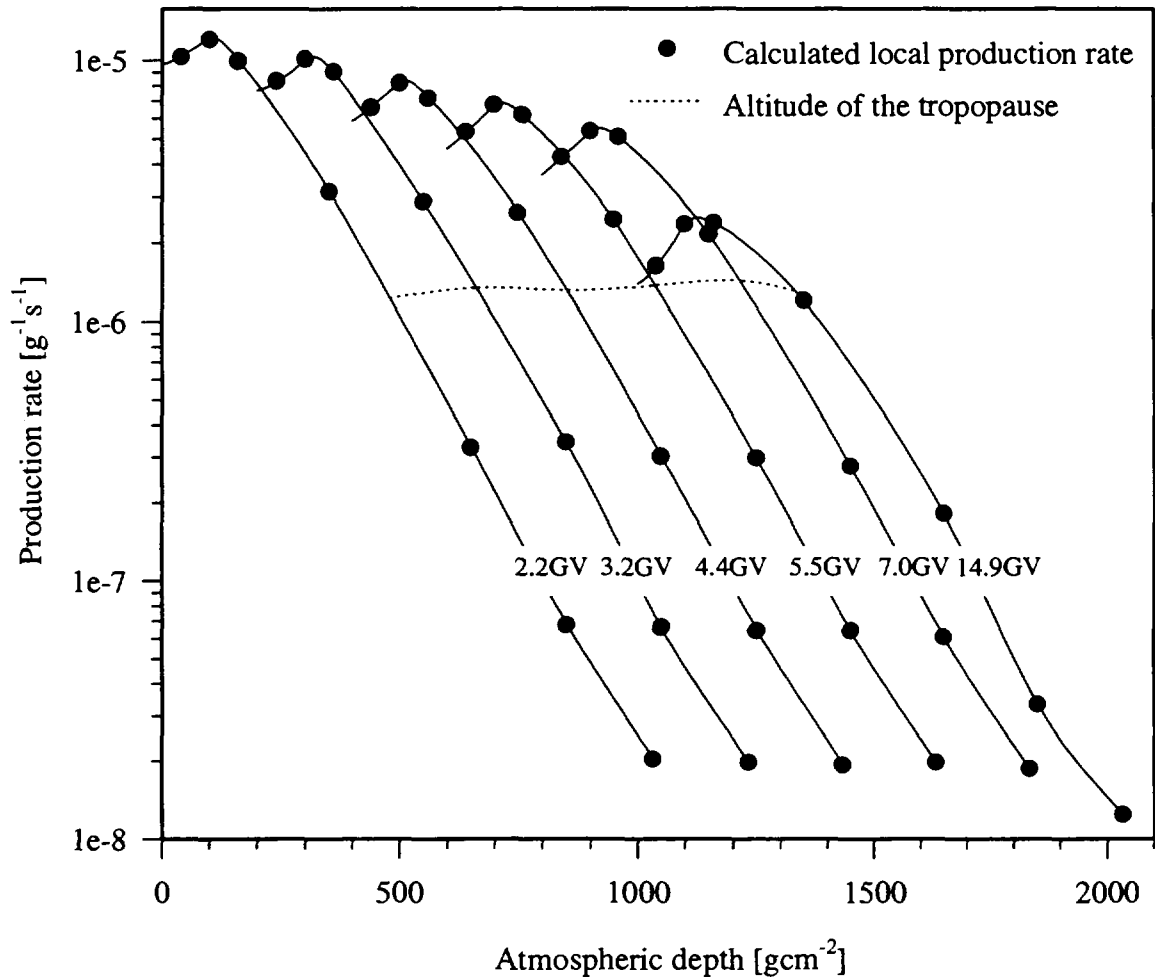


Figure 4.5: Dependence of the ^{36}Cl atmospheric production rate as a function of altitude at mean solar activity. The x-axis applies to the curve for $R_{\text{c}}=2.2$ GV, while the other curves corresponding to increasing cutoff rigidities are displaced along the x-axis by a value of 200 gcm^{-2} each.

The neutron flux spectra of Armstrong et al. (1973) were used for a calculation only at one latitude, corresponding to a cutoff rigidity of 4.5 GV and at 10 altitudes (0, 5, 10, 50, 100, 200, 400, 600, 800 and 1033 gcm^{-2}). The local production rates for the reaction $^{36}\text{Ar}(n,p)^{36}\text{Cl}$ were then calculated only at this latitude and compared to the production rates for the two other reactions with protons and neutrons at 4.4 GV. For all altitudes, the ratio of the production rate via the reaction $^{36}\text{Ar}(p,n)^{36}\text{Cl}$ to the total production rate was about 0.075. Therefore, for all latitudes, only the production rates from the reactions $^{40}\text{Ar}(p,X)^{36}\text{Cl}$ and $^{40}\text{Ar}(n,p4n)^{36}\text{Cl}$ were calculated and the

results were multiplied by the correction factor of 1.075. The resulting 42 local production rates are plotted in figure 4.5.

In a second step, the ^{36}Cl atmospheric production rates were calculated by integrations of the curves shown in figure 4.5 to obtain its latitudinal dependence.

$$P_j(R_{cv}) = \int_h P_j(R_{cv}, h) \cdot dh \quad (4.4)$$

This integration was carried out in such a way, that both tropospheric and stratospheric production rates were calculated independently. The atmospheric production rate of ^{36}Cl as a function of the latitude is shown in figure 4.6.

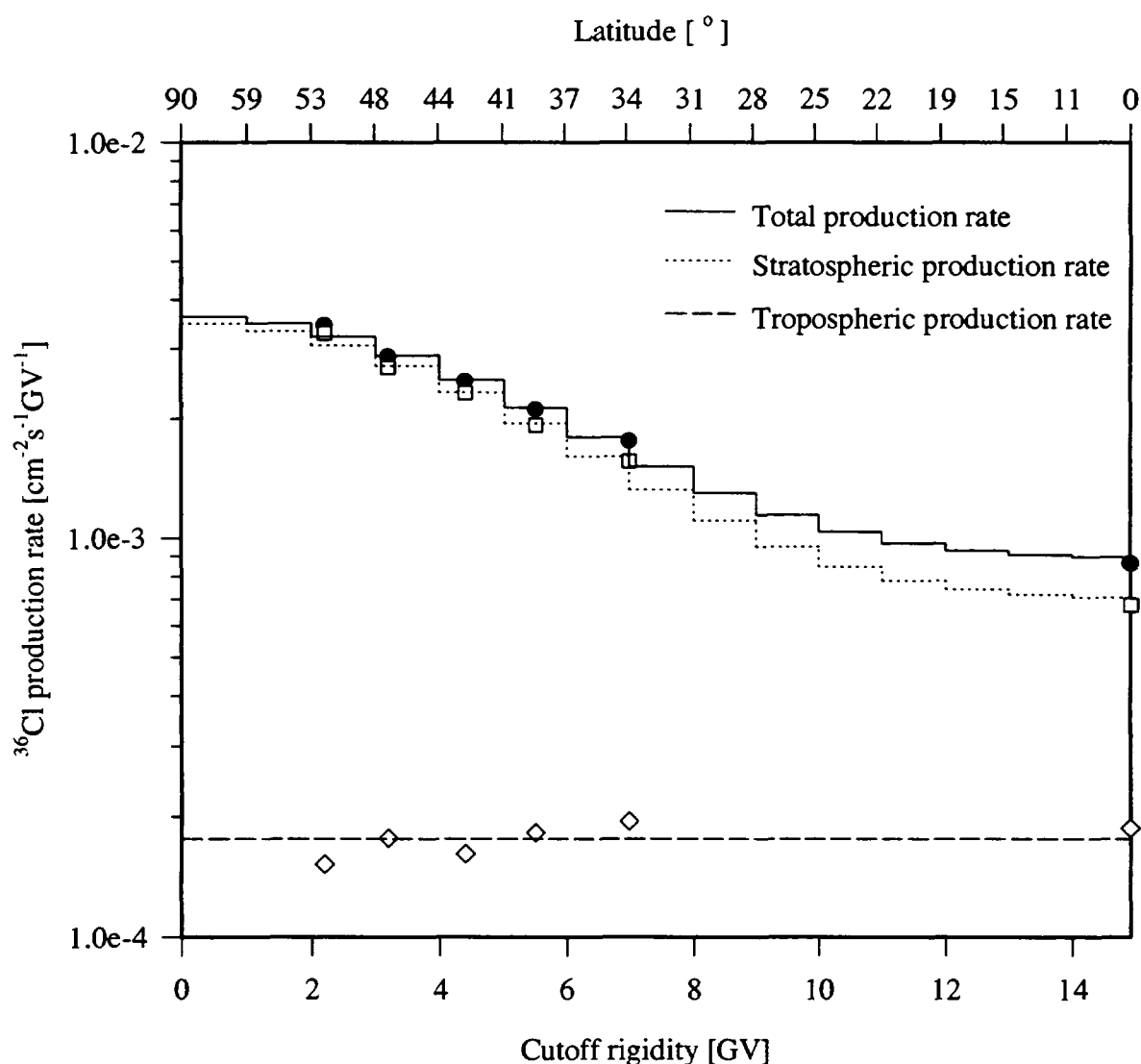


Figure 4.6: Latitudinal dependence of the ^{36}Cl atmospheric production rate at mean solar activity. The symbols correspond to the calculated values whereas the curves are the best fits through these points.

Figure 4.6 shows that only the stratospheric production of ^{36}Cl is affected by the earth geomagnetic field, the production being lower at the equator than at the poles. The tropospheric production is constant and independent of latitude.

Table 4.1 summarizes the results for the ^{36}Cl production rates. Only 7% of the total ^{36}Cl production occurs in the troposphere. This result disagrees with the estimate of 33% from Lal and Peters (1967). About 8 % of the total production is found to be due to the reaction $^{36}\text{Ar}(n,p)^{36}\text{Cl}$. The same value has been found by Huggle et al. (1996) using the same reaction cross sections, but other neutron fluxes (Hess et al., 1959).

Table 4.1: Production rates of ^{36}Cl for mean solar activity.

Target	Production rate [$\text{m}^{-2}\text{s}^{-1}$]		
	Troposphere	Stratosphere	Atmosphere
^{36}Ar	0.2	1.2	1.4
^{40}Ar	1.7	16.9	18.6
Total	1.9	18.1	20.0

As shown in Table 4.2, the production rate of $20 \text{ m}^{-2}\text{s}^{-1}$ obtained in this work is in good agreement with an early value of Oeschger et al. (1970) and with the recent value obtained by Huggle et al. (1996), who used roughly identical cross sections as in this work, but calculated the production rate only for one latitude. Our value is higher by a factor of two compared to other values, which were calculated by the same method as in this work, i.e., taking into account local production rates at different points of the atmosphere (Lal and Peters, 1967; O'Brien, 1979; Masarik and Reedy, 1995).

Table 4.2: Comparison of calculated production rates of ^{36}Cl (mean solar activity).

Production rate [$\text{m}^{-2}\text{s}^{-1}$]	Reference
11	Lal and Peters, 1967
22	Oeschger et al., 1962
8.7	O'Brien, 1979
12	Masarik and Reedy, 1995
19	Huggle et al., 1996
20	This work

4.2 Deposition rates of ^{36}Cl

After production, the ^{36}Cl atoms are distributed homogeneously in the stratosphere, then enter the troposphere and deposit on the Earth surface through wet and dry deposition. For the application of ^{36}Cl to Earth sciences, the deposition rate as a function of latitude is one of the most important parameter needed to be known.

The ^{36}Cl atoms produced in the troposphere are supposed to be deposited at the same latitude where they were produced. This assumption may be incorrect. If distribution of ^{36}Cl in the troposphere is fast, the deposition at a given latitude could depend on the amount of precipitation. With respect to the ^{36}Cl atoms produced in the stratosphere, Lal and Peters (1967) used the bomb-produced ^{90}Sr fallout to model the transfer of cosmogenic nuclides to the troposphere and their subsequent deposition. This latitudinal dependence was multiplied with the production rate calculated in this work to predict the deposition rates of ^{36}Cl . The results are shown in figure 4.7 and compared with measured deposition data.

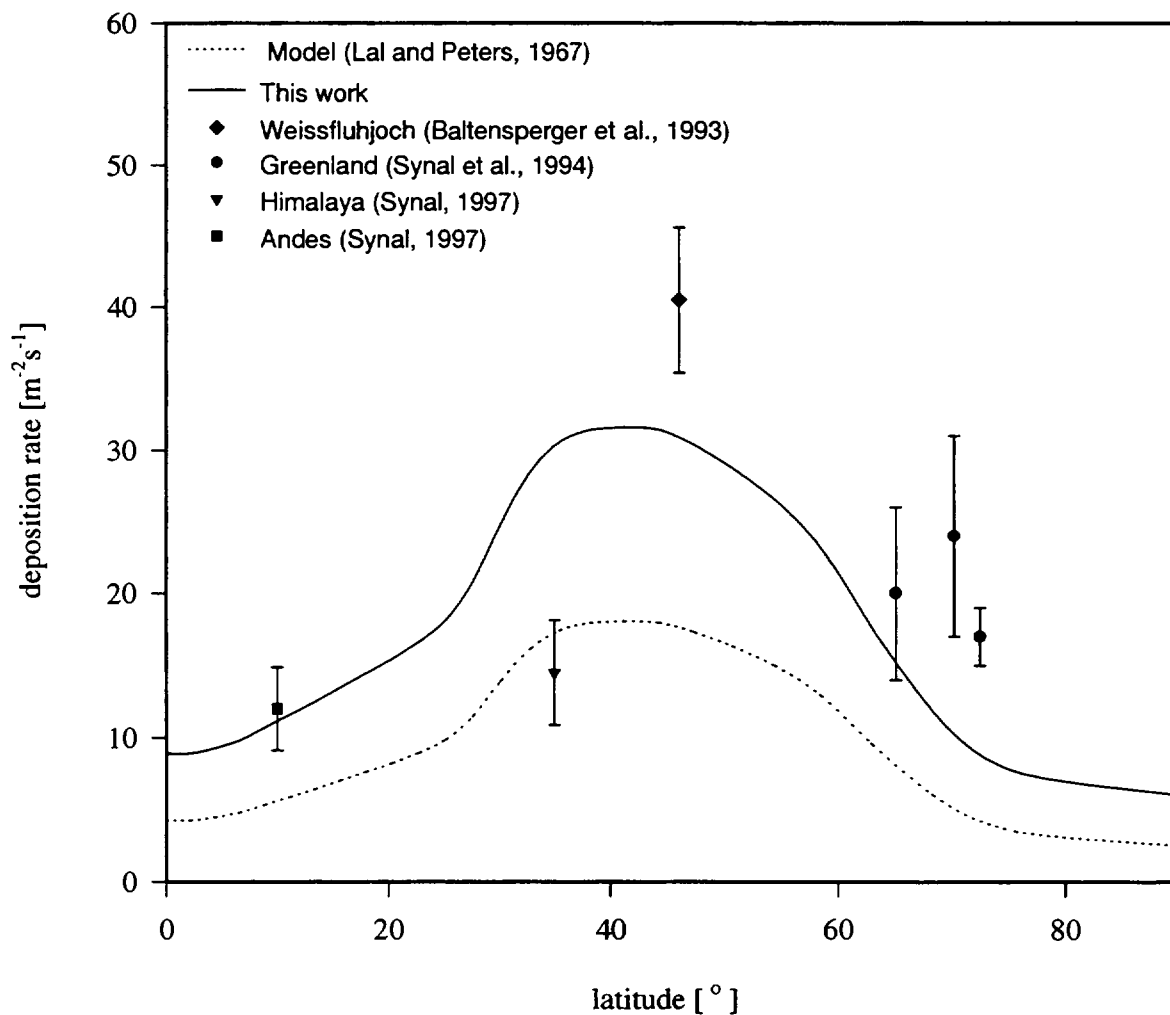


Figure 4.7: Deposition rates of ^{36}Cl as a function of the latitude.

The measured data agree better with the model from this work compared to the model of Lal and Peters (1967). This is mainly due to the difference between the calculated production rates (see Table 4.2). However, both theoretical deposition rates generally underestimate observed deposition rates. It is therefore important to concentrate future efforts on a calculation of the production rate of ^{36}Cl induced by solar cosmic rays. Since high cross sections were measured in the 15-100 MeV energy range, this production could be important. Moreover, atmospheric speciation of ^{36}Cl should be carried out. Effectively, gaseous H^{36}Cl could be produced which has a different atmospheric behavior than ^{90}Sr . Finally, it seems likely that the local precipitation rates affect the deposition rate, i.e. for a given latitude, a higher deposition might occur at sites with high precipitation amounts compared to those with lower ones.

4.3 Conclusions

A new calculation of the atmospheric production rate of ^{36}Cl induced by galactic cosmic rays has been carried out resulting in a value of $20\text{m}^{-2}\text{s}^{-1}$. This value confirms an early estimate made by Oeschger et al. (1969), but is a factor of two higher than the most frequently used value of Lal and Peters (1967). However, based on the high cross sections of the reaction $^{40}\text{Ar}(p,X)^{36}\text{Cl}$ measured in the 15-100 MeV energy range, the contribution of solar cosmic rays to the ^{36}Cl production rate might be high and should be quantified in the future.

A latitudinal deposition rate model was proposed. It depends only on the calculated ^{36}Cl production rate and on the observed fallout of bomb-produced ^{90}Sr . Slight disagreements are found between predicted and measured deposition rates. This shows that a more detailed model has to be developed to better explain the ^{36}Cl deposition rates. For example, local conditions, such as precipitation rates have to be included in such models.

References

- Alburger, D.E., Harbottle, G., Norton, E.F. (1986) Half-life of ^{32}Si , *Earth Planet. Sci. Lett.*, **78**, 168-176.
- Aleksandrov, V.N., Semenova, M.P., Semenov, V.G. (1987) (p,x) reaction cross sections of radionuclides production on copper and nickel, *At. Energ.*, **62**, 411-413.
- Allkofer, O.C. and Grieder, P.K.F. (1984) Cosmic Rays on the Earth, in: *Physics Daten*, vol. **25/1**, Fachinformationzentrum Energie - Physik - Mathematik GMBH, Karlsruhe, pp. 1-377.
- Armstrong, T.W., Chandler, K.C., Barish, J. (1973) Calculations of neutron flux spectra induced in the Earth's atmosphere by galactic cosmic rays, *J. Geophys. Res.*, **78**, 2715-2726.
- Baker, E., Friedlander, G., Hudis, J. (1958) Formation of Be^7 in interactions of various nuclei with high-energy protons, *Phys. Rev.*, **112**, 1319-1321.
- Baltensperger, U., Schwikowski, M., Gäggeler, H.W., Jost, D.T., Beer, J., Siegenthaler, U., Wagenbach, D., Hofmann, H.J., Synal, H.-A. (1993) Transfer of atmospheric constituents into an Alpine snow field, *Atmos. Environ.*, **27A**, 1881-1890.
- Barber, H.B., Bowen, T., Delise, D.A., Jenkins, E.W., Jones, J.J., Kalbach, R.M., Pifer, A.E. (1980) Predictions and measurements of mass spectra of the charged nucleonic component of cosmic rays at mountain altitude, *Phys. Rev.*, **D22**, 2667-2687.
- Beer, J., Bonani, G., Hofmann, H.J., Suter, M., Synal, H.A., Wölfli, W., Oeschger, H., Siegenthaler, U., Finkel, R.C. (1987) ^{10}Be measurements on polar ice - comparison of Arctic and Antarctic records, *Nucl. Instr. and Meth.*, **B29**, 203-206.
- Beer, J., Blinov, A., Bonani, G., Finkel, R.C., Hofmann, H.J., Lehmann, B., Oeschger, H., Sigg, A., Schwander, J., Staffelbach, T., Stauffer, B., Suter, M., Wölfli, W. (1990) Use of ^{10}Be in polar ice to trace the 11-year cycle of solar activity, *Nature*, **347**, 164-166.
- Bertini, H.W. (1969) Intranuclear-cascade calculation of the secondary nucleon spectra from nucleon-nucleus interactions in the energy range 340 to 2900 MeV and comparisons with experiment, *Phys. Rev.*, **188**, 1711-1730.
- Bhandari, N., Nijampurkar, V.N., Vohra, C.P. (1981) Radiometric chronology of some Himalayan glaciers, in: *Proc. Symp. on Variations in the Global Water Budget*, A. Street-Perrott, M. Beran, R. Ratcliffe (eds.), Reidel, Dordrecht, pp. 207-220.

- Bodemann, R., Lange, H.-J., Leya, I., Michel, R., Schieckel, T., Rössel, R., Herpers, U., Hofmann, H.J., Dittrich, B., Suter, M., Wölfli, W., Holmqvist, B., Condé, H., Malmborg, P. (1993) Production of residual nuclei by proton-induced reactions on C, N, O, Mg, Al and Si, *Nucl. Instr. and Meth.*, **B82**, 9-31.
- Brooke, G. and Wolfendale, A.W., The momentum spectrum of cosmic ray protons near sea level in the momentum range 0.6-150 GeV/c, *Proc. Phys. Soc.*, **83**, 843-851.
- Brown, L., Stensland, G.J., Klein, J., Middleton, R. (1989) Atmospheric deposition of ^7Be and ^{10}Be , *Geochim. Cosmochim. Acta*, **53**, 135-142.
- Chen, Y., Kashy, E., Bazin, D., Benenson, W., Morissey, D.J., Orr, N.A., Sherrill, B.M., Winger, J.A., Young, B., Yurkon, J. (1993) Half-life of ^{32}Si , *Phys. Rev.*, **C47**, 1462-1465.
- Clausen, H.B. (1973) Dating of polar ice by ^{32}Si , *J. Glaciology*, **12**, 411-416.
- Cumming, J.B. (1983) Assay of ^{32}Si by liquid scintillation counting, *Radiochem. Radioanal. Lett.*, **58**, 297-306.
- Dansgaard, W., Clausen, H.B., Aarkrog, A. (1966) Evidence for bomb-produced silicon 32, *J. Geophys. Res.*, **71**, 5474-5477.
- Dansgaard, W., Clausen, H.B., Aarkrog, A. (1966) The Si^{32} fallout in Scandinavia, *Tellus*, **18**, 187-191.
- Davis, E.A., Bonner, T.W., Worley, D.M., Bass, R. (1964) The disintegration of ^{36}Ar and ^{40}Ar by neutrons, *Nucl. Phys.*, **55**, 643-656.
- DeMaster, D.J. and Cochran, J.K. (1982) Particle mixing rates in deep-sea sediments determined from excess ^{210}Pb and ^{32}Si profiles, *Earth Planet. Sci. Lett.*, **61**, 257-271.
- Döcher, A. (1996) Historische Entwicklung von atmosphärischen Spurenstoffkonzentrationen rekonstruiert aus Firm und Eis alpiner Gletscher, Ph. D. Thesis, University of Berne, Switzerland.
- Elmore, D., Anantaraman, N., Fulbright, H.W., Gove, H.E., Hans, H.S., Nishiizumi, K., Murell, M.T., Honda, M. (1980) Half-life of ^{32}Si from Tandem-Accelerator Mass Spectrometry, *Phys. Rev. Lett.*, **45**, 589-592.
- Elmore D., Conard, N.J., Kubik, P.W., Gove, H.E., Wahlen, M., Beer, J., Suter, M. (1987) ^{36}Cl and ^{10}Be profiles in Greenland ice: dating and production rate variations, *Nucl. Instr. and Meth.*, **B29**, 207-210.
- Epherre, M. and Seide, C. (1971) Excitation functions of ^7Be and ^{11}C produced in nitrogen by low-energy protons, *Phys. Rev.*, **C3**, 2167-2171.
- Filthuth, H. (1955) Das Energiespektrum der Protonen in der Höhenstrahlung auf Seehöhe, *Z. Naturforschg.*, **A10**, 219-229.

- Fink, D., Sisterson, J., Vogt, S., Herzog, G., Klein, J., Middleton, R., Koehler, A., Magliss, A. (1990) Production of Ca-41 and K, Sc and V short-lived isotopes by the irradiation of Ti with 35 to 150 MeV protons - applications to solar cosmic-ray studies, *Nucl. Instr. and Meth.*, **B52**, 601-607.
- Finkel, R.C. and Suter, M. (1993) AMS in the Earth Sciences: Technique and Applications, in: *Advances in Analytical Geochemistry*, vol. 1, Marian Hyman (ed.), Jai-Press, Greenwich, pp. 1-114.
- Flückiger, E. (1976) Ein Programmsystem zur Beschreibung der Wechselwirkung zwischen hochenergetischen Nukleonen und Materie und seine Anwendung bei kosmischen Strahluntersuchungen, Physikalisches Institut, University of Berne, Switzerland, unpublished.
- Franke, T., Fröhlich, K., Gellermann, R., Herbert, D. (1986) ^{32}Si in precipitation of Freiberg (GDR), *J. Radioanal. Nucl. Chem. Lett.*, **103**, 11-17.
- Fröhlich, K., Franke, T., Gellermann, R.; Herbert, D. (1988) Studies of ^{32}Si in different aquifers and implications for groundwater dating, *Isotopenpraxis*, **24**, 355-363.
- Gäggeler, H.W., von Gunten, H.R., Rössler, E., Oeschger, H., Schotterer, U. (1983) ^{210}Pb -dating of cold alpine firm/ice cores from Colle Gnifetti, Switzerland, *J. Glaciol.*, **29**, 165-177.
- Gardner, D. and Rosenblum, S. (1967) Trends in nuclear reaction cross sections, *Nucl. Phys.*, **A96**, 121-137.
- Gavini, M.B., Beck, J.N., Kuroda, P.K. (1974) Mean residence times of long-lived radon daughters in the atmosphere, *J. Geophys. Res.*, **79**, 4447-4452.
- Geant Code (1993) Detector description and simulation tool, CERN Program Library Long Writeups Q123.
- Geithof, D. (1962) Über die Herstellung von Si^{32} durch einen (t,p)-Prozess, *Radiochim. Acta*, **1**, 3-6.
- Gellerman, R., Börner, I., Franke, T., Fröhlich, K. (1988) Preparation of water samples for ^{32}Si determinations, *Isotopenpraxis*, **24**, 114-117.
- Hess, W.N., Patterson, H.W., Wallace, R., Chupp, E.L. (1959) Cosmic-ray neutron energy spectrum, *Phys. Rev.*, **116**, 44-457.
- Hofmann, H.J., Bonani, G., Suter, M., Wölfli, W., Zimmermann, D., von Gunten, H.R. (1990) A new determination of the half-life of ^{32}Si , *Nucl. Instr. and Meth.*, **B52**, 544-551.
- Honda, M. and Lal, D. (1964) Spallation cross sections for long-lived radionuclides in iron and light nuclei, *Nucl. Phys.*, **51**, 363-368.
- Huggle, D., Blinov, A., Stan-Sion, C., Korschinek, G., Scheffel, C., Massonet, S., Zerle, L., Beer, J., Parrat, Y., Gäggeler, H.W., Hajdas, W., Nolte, E. (1996) Production of cosmogenic ^{36}Cl on atmospheric argon, *Planet. Space Sci.*, **44**, 147-151.

- Ilijin, A.S., Semenov, V.G., Semenova, M.P., Sobolevsky, N. M., Udovenko, L.V. (1991) Interactions of protons with targets from He to Br. In: *Landolt-Börnstein New Series, Numerical Data and Functional Relationships in Science and Technology*, Group I, vol. **13a**, H. Schopper (ed.), Springer Verlag, Berlin, p. 32.
- Jantsch, K. (1967) Kernreaktionen mit Tritonen beim ^{30}Si , 3. Mitteilung: Bestimmung der Halbwertszeit von ^{32}Si , *Kernenergie*, **10**, 89-91.
- Jiang, S.S., Hemmick, T.K., Kubik, P.W., Elmore, D., Gove, H.E., Tullai-Fitzpatrick, S. (1990) Measurements of the $^{36}\text{Ar}(n,p)^{36}\text{Cl}$ cross section at thermal energies using the AMS technique, *Nucl. Instr. and Meth.*, **B52**, 608-611.
- Kharkar, D.P., Nijampurkar, V.N., Lal, D. (1966) The global fallout of ^{32}Si produced by cosmic rays, *Geochim. Cosmochim. Acta*, **30**, 621-631.
- Koch, U. (1982) ^{32}Si -Aktivitätsmessungen an natürlichen Wässern, Ph.D. Thesis, TU Bergakademie Freiberg, Germany.
- Kocharian, N.M., Saakian, G.S., Kirakosian, Z.A. (1959) Energy spectra and nuclear interactions of cosmic-ray particles, *Sov. Phys. JETP*, **35**, 933-942.
- Kutschera, W., Henning, W., Paul, M., Smither, R.K., Stephenson, E.J., Yntema, J.L., Alburger, D.E., Cumming, J.B., Harbottle, G. (1980) Measurement of the ^{32}Si half-life via Accelerator Mass Spectrometry, *Phys. Rev. Lett.*, **45**, 592-596.
- Lal, D. and Peters, B. (1967) Cosmic ray produced radioactivity on the Earth, in: *Handbook of Physics*, vol. **46/2**, E.U. Condon and H. Odishaw (eds.), McGraw-Hill, New York, pp. 551-612.
- Lal, D., Nijampurkar, V.N., Rajagopalan, G., Somayajulu, B.L.K. (1979) Annual fallout of ^{32}Si , ^{210}Pb , ^{22}Na , ^{35}S and ^7Be in rains in India, *Proc. Indian Acad. Sci.*, **88A**, 29-40.
- Lal, D. and Somayajulu, B.L.K. (1984) Some aspects of the geochemistry of silicon isotopes, *Tectonophysics*, **105**, 383-397.
- Machta, L. and List, R.J. (1959) Transport in the stratosphere and through the tropopause, *Adv. Geophys.*, **6**, 273-288.
- Masarik, J. (1996) Private communication.
- Masarik, J. and Reedy R.C. (1995) Terrestrial cosmogenic-nuclide production systematics calculated from numerical simulations, *Earth Planet. Sci. Lett.*, **136**, 381-395.
- Merker, M. (1973) The contribution of galactic cosmic rays to the atmospheric neutron maximum dose equivalent as a function of neutron energy and altitude, *Health Phys.*, **25**, 524-527.
- Michel, R., Weigel, H., Herr, W. (1978) Proton-induced reactions on nickel with energies between 13 and 45 MeV, *Z. Phys.*, **A286**, 393-400.

- Michel, R., Dragovitsch, P., Englert, P., Peiffer, F., Stück, R., Theis, S., Begemann, F., Weber, H., Signer, P., Wieler, R., Filges, D., Cloth, P. (1986) On the depth dependence of spallation reactions in a spherical thick diorite target homogeneously irradiated by 600 MeV protons - simulation of production of cosmogenic nuclides in small meteorites, *Nucl. Instr. and Meth.*, **B16**, 61-82.
- Michel, R. and Blann, M. (1993) private communication.
- Morgenstern, U., Taylor, C.B., Parrat, Y., Gäggeler, H.W., Eichler, B. (1996) ^{32}Si in precipitation: temporal and spatial variation and ^{32}Si as dating tool for glacial ice, *Earth Planet. Sci. Lett.*, **144**, 289-296.
- Mylroie, M.G. and Wilson, J.G. (1951) On the proton component of the vertical cosmic-ray beam at sea level, *Proc. Phys. Soc.*, **A64**, 404-417.
- Nijampurkar, V.N., Bhandari, N., Vohra, C.P., Krishnan, V. (1982) Radiometric chronology of Nehrur glacier, *J. Glaciol.*, **28**, 91-105.
- Nijampurkar, V.N. and Rao, D.K. (1993) Polar fallout of radionuclides ^{32}Si , ^7Be and ^{210}Pb and past accumulation rate of ice at Indian station, Dakshin Gangotri, east Antarctica, *J. Environ. Radioact.*, **21**, 107-117.
- Nydal, R. (1968) Further investigation on the transfer of radiocarbon in nature, *J. Geophys. Res.*, **73**, 3617-3635.
- O'Brien, K. (1979) Secular variations in the production of cosmogenic isotopes in the Earth's atmosphere, *J. Geophys. Res.*, **84**, 423-431
- Oeschger H., Houtermans J., Loosli H. Wahlen M. (1969) The constancy of cosmic radiation from isotope studies in meteorites and on the Earth, in: *Radiocarbon Variations and Absolute Chronology, 12th Nobel Symp.*, I.U. Olsson (ed.), Interscience New York, pp. 471-496.
- Prael, R.E. and Bozoian, M. (1988) Adaptation of the multistage preequilibrium model for the Monte-Carlo Method, LANL-preprint LA-UR-88-3238.
- Preszler, A.M., Simnet, G.M., White, R.S. (1974) Angular distribution and altitude dependence of atmospheric neutrons from 10 to 100 MeV, *J. Geophys. Res.*, **79**, 17-22.
- Rayudu, G.V.S. (1964) Formation cross sections of various radionuclides from Ni, Fe, Si, Mg, O and C for protons of energies between 130 and 400 MeV, *Can. J. Chem.*, **42**, 1149-1154.
- Reedy, R.C., Arnold, J.R., Lal, D. (1983) cosmic-ray record in solar system matter, *Ann. Rev. Nucl. Part. Sci.*, **33**, 505-537.
- Reiter, R., Munzert, K., Kanter, H.-J., Pötzl, K. (1983) Cosmogenic radionuclides and ozone at a mountain station at 3.0 km a.s.l., *Arch. Meteorol. Geophys. Bioclimatol.*, **32B**, 131-160.
- Rudstam, G. (1966) Systematics of spallation yields, *Z. Naturforsch.*, **21a**, 1027-1041.

- Schiekel, T., Sudbrock, F., Herpers, U., Gloris, M., Lange, H.-J., Leya, I., Michel, R., Dittrich-Hannen, B., Synal, H.-A., Suter, M., Kubik, P.W., Blann, M., Filges, D. (1996) Nuclide production by proton-induced reactions on elements ($6 \leq Z \leq 29$) in the energy range from 200 to 400 MeV, *Nucl. Instr. and Meth.*, **B114**, 91-119.
- Schwikowski, M., Seibert, P., Baltensperger, U., Gäggeler, H.W. (1995) A study of an outstanding Saharan dust event at the high-alpine site Jungfrauoch, Switzerland, *Atmos. Environ.*, **29A**, 1829-1842.
- Silberberg, R. and Tsao, C.H. (1973) Partial cross-sections in high-energy nuclear reactions, and astrophysical applications. I. Target with $Z \leq 28$, *The Astrophysical Journal Supplement Series*, **25**, 315-333.
- Somayajulu, B.L.K., Rengarajan, R., Lal, D., Weiss, R.F., Craig, H. (1987) GEOSECS Atlantic ^{32}Si profiles, *Earth Planet. Sci. Lett.*, **85**, 329-342.
- Steyn, G.F., Mills, S.J., Nortier, F.M., Simpson, B.R.S., Meyer, B.R. (1990) Production of ^{52}Fe via proton-induced reactions on manganese and nickel, *Appl. Radiat. Isot.*, **41**, 315-325.
- Surbeck, H. and Ferreri, G. (1994) Allgemeine Überwachung: Luft, Niederschläge, Flusswasser, Boden, Gras, in: *Environmental Radioactivity and Radiation Exposure in Switzerland in 1993*, Federal Office of Public Health, Switzerland, pp. 3.1.1-3.1.11.
- Suter, M., Beer, J., Bonani, G., Hofmann, H.J., Michel, D., Oeschger, H., Synal, H.-A., Wölfli, W. (1987) ^{36}Cl studies at the ETH/SIN-AMS facility, *Nucl. Instr. and Meth.*, **B29**, 211-214.
- Synal, H.-A., Beer, J., Bonani, G., Suter, M., Wölfli, W. (1990) Atmospheric transport of bomb-produced ^{36}Cl , *Nucl. Instr. and Meth.*, **B52**, 483-488.
- Synal H.-A., Beer J., Bonani G., Lukasczyk C. and Suter M. (1994) ^{36}Cl measurements at the Zürich AMS facility, *Nucl. Instr. and Meth.*, **B92**, 79-84.
- Synal, H.-A. (1997) Private communication.
- Tanaka, S., Furukawa, M., Chiba, M. (1972) Nuclear reactions of nickel with protons up to 56 MeV, *J. Inorg. Nucl. Chem.*, **34**, 2419-2426.
- Tarkanyi, F., Szelecsenyi, F., Popecky, P. (1991) Excitation functions of proton induced nuclear reactions on natural nickel for monitoring beam energy and intensity, *Appl. Radiat. Isot.*, **42**, 513-517.
- Thomsen, M.S., Heinemeier, J., Hornshøj, P., Nielsen, H.L., Rud, N. (1991) Half-life of ^{32}Si measured via Accelerator Mass spectrometry, *Nucl. Phys.*, **A534**, 327-338.
- Tobailem, J., de Lassus St. Genies, C., Leveque, L. (1981) Sections efficaces des réactions nucléaires induites par protons, deutons, particules Alpha - V. Silicium, *Note CEA-N-1466 (5)*, 106-120.

- Turkevich, A. and Samuels, A. (1954) Evidence for Si^{32} , a long-lived beta emitter, *Phys. Rev.*, **94**, 364.
- Ziegler, J.F., Cuomo, G., Biersack, J.P. (1988) TRIM-88, computer program.
- Zimmermann, D. and von Gunten, H.R. (1996) Chemical-sample preparation for the determination of ^{32}Si by accelerator mass-spectrometry, *Radiochim. Acta*, **72**, 97-100.
- Zoppi, U., Kubik, P.W., Suter, M., Synal, H.-A., Von Gunten, H.R., Zimmermann, D. (1994) High-intensity isobar separation at the Zurich AMS facility, *Nucl. Instr. and Meth.*, **B92**, 142-145.

Acknowledgements

I would like to thank Prof. Dr. H.W. Gäggeler who gave me the possibility to work in his team and to enlarge my knowledge in radiochemistry and Dr. U. Baltensperger for solving many problems in fruitful discussions.

I highly appreciate the help of Dr. W. Hajdas, operator of the PIF facility, during all beam times. His experience in proton flux measurements was of great help.

Prof. Dr. E. Flückiger, from the Physics Institute of University of Bern, who left his calculation model of protons and neutrons atmospheric intensities at my disposal is greatly appreciated.

I also thank the Accelerator Mass Spectrometry group of the ETH of Zurich, especially Dr. H.A. Synal, Dr. P.W. Kubik and Dr. M. Suter for the ^{36}Cl and ^{10}Be measurements.

The chemical extraction of ^{36}Cl and ^{10}Be from the gas targets was carried out at the EAWAG in Dübendorf. I would like to thank Dr. J. Beer and his group for their help and fruitful discussions.

The interest of Prof. Dr. H.R. von Gunten in my work was very stimulating for me as well as the help of Prof. Dr. B. Eichler in solving problems of chemical nature.

Mrs. S. Brüttsch and Mr. R. Keil have carried out many chemical analyses of my samples and are also highly acknowledged.

I also would also like to thank all the persons who helped me during the gas target bombardments: Dr. A. Döscher, Dr. M. Schwikowski, T. Döring, R. Dressler, D. Huggle, Dr. D. Jost, M. Kalberer, Dr. A. Türler and Dr. P. Zimmermann.

Last but not least, the free access at the research station of the Jungfrauoch is highly appreciated, as well as the help of Dr. U. Baltensperger, Prof. Dr. B. Eichler, Dr. S. Hübener, O. Joss, M. Lugauer, Dr. U. Morgenstern and O. Nitsche in helping to collect enormous amounts of fresh snow.

This thesis work was supported by the Paul Scherrer Institute.

Curriculum vitae

I was born on the 2nd of December 1967 in Delémont as the son of Roland Parrat and Christine, born Cattin. I lived during 20 years in Soyhières, where I accomplished the primary school between 1974 and 1978. I followed the secondary school classes in Delémont until 1983. In 1983, I moved to lycée cantonal of Porrentruy, where I obtained the matura of type C in 1987. In the same year, I started my chemistry study at EPF-Lausanne, where I obtained the diploma as a chemistry engineer in January 1992. In February 1993, I began a Ph. D. Thesis at the Paul Scherrer Institute and at the Institute of Inorganic, Analytic and Physical Chemistry of the University of Berne under the guidance of Prof. Dr. H.W. Gäggeler. On the 13th of Mai 1995, I married Françoise Spiess who gave me a son, named Tristan, on the 10th of February 1997.